



# Particle transport and deposition in wall-sheared thermal turbulence

Ao Xu<sup>1,2,3</sup>, Ben-Rui Xu<sup>1</sup> and Heng-Dong Xi<sup>1,2,3,†</sup>

<sup>1</sup>School of Aeronautics, Northwestern Polytechnical University, Xi'an 710072, PR China

<sup>2</sup>Institute of Extreme Mechanics, Northwestern Polytechnical University, Xi'an 710072, PR China

<sup>3</sup>National Key Laboratory of Aircraft Configuration Design, Xi'an 710072, PR China

(Received 21 March 2024; revised 17 July 2024; accepted 9 September 2024)

We studied the transport and deposition behaviour of point particles in Rayleigh–Bénard convection cells subjected to Couette-type wall shear. Direct numerical simulations (DNSs) are performed for Rayleigh number ( $Ra$ ) in the range  $10^7 \leq Ra \leq 10^9$  with a fixed Prandtl number  $Pr = 0.71$ , while the wall-shear Reynolds number ( $Re_w$ ) is in the range  $0 \leq Re_w \leq 12\,000$ . With the increase of  $Re_w$ , the large-scale rolls expanded horizontally, evolving into zonal flow in two-dimensional simulations or streamwise-oriented rolls in three-dimensional simulations. We observed that, for particles with a small Stokes number ( $St$ ), they either circulated within the large-scale rolls when buoyancy dominated or drifted near the walls when shear dominated. For medium  $St$  particles, pronounced spatial inhomogeneity and preferential concentration were observed regardless of the prevailing flow state. For large  $St$  particles, the turbulent flow structure had a minor influence on the particles' motion; although clustering still occurred, wall shear had a negligible influence compared with that for medium  $St$  particles. We then presented the settling curves to quantify the particle deposition ratio on the walls. Our DNS results aligned well with previous theoretical predictions, which state that small  $St$  particles settle with an exponential deposition ratio and large  $St$  particles settle with a linear deposition ratio. For medium  $St$  particles, where complex particle–turbulence interaction emerges, we developed a new model describing the settling process with an initial linear stage followed by a nonlinear stage. Unknown parameters in our model can be determined either by fitting the settling curves or using empirical relations. Compared with DNS results, our model also accurately predicts the average residence time across a wide range of  $St$  for various  $Re_w$ .

**Key words:** Bénard convection, particle/fluid flow, turbulent convection

† Email address for correspondence: [hengdongxi@nwpu.edu.cn](mailto:hengdongxi@nwpu.edu.cn)

## 1. Introduction

Turbulence significantly affects the dynamics of particulate suspensions, as evidenced ubiquitously in nature and daily life (Guha 2008; Toschi & Bodenschatz 2009; Mathai, Lohse & Sun 2020; Brandt & Coletti 2022). For example, aeolian processes can lead to the airborne movement or saltation of sand grains of different sizes under the influence of wind, triggering dust storms, especially under unstable thermal conditions (Zheng 2009; Zhang 2024). Another example is the use of heating, ventilation and air conditioning systems, which can extend the suspension duration and spread of respiratory droplets, with this effect amplified by air currents in indoor environments (Mittal, Ni & Seo 2020; Hedworth *et al.* 2021). In these scenarios, buoyancy forces generated by temperature differences drive turbulent flows. To study thermal turbulence, the Rayleigh–Bénard (RB) convection system serves as a canonical paradigm. This system involves a fluid layer heated from the bottom and cooled from the top (Ahlers, Grossmann & Lohse 2009; Lohse & Xia 2010; Chillà & Schumacher 2012; Wang, Zhou & Sun 2020a; Xia *et al.* 2023). The control parameters in the RB system include the Prandtl number ( $Pr$ ), which describes a fluid's thermophysical properties, and the Rayleigh number ( $Ra$ ), which describes the relative strength of buoyancy forces vs thermal and viscous dissipation. In RB turbulent convection, ubiquitous coherent structures include small-scale plumes and large-scale circulation (LSC). After detaching from the boundary layers, sheet-like plumes transform into mushroom-like plumes through mixing and clustering (Zhou, Sun & Xia 2007). Through plume–vortex and plume–plume interactions, thermal plumes further self-organize into the LSC, which spans the whole convection cell (Xi, Lam & Xia 2004).

Due to these complex multi-scale coherent structures of thermal turbulence, efforts have been devoted to investigating the transport and deposition behaviour of particles in thermal convection. A particularly interesting aspect is the spatial distribution and deposition rate of particles in thermal turbulence. Depending on the Stokes number ( $St$ ), which describes the particle inertia relative to that of the fluid, the particles' dynamic behaviour can be classified into three categories. For particles with a small  $St$ , they are randomly distributed and behave like tracer particles; in the limit of infinitely small  $St$ , they exhibit an exponential deposition rate (Martin & Nokes 1989). For particles with a large  $St$ , their motion is almost unaffected by the underlying thermal turbulence; in the limit of infinitely large  $St$ , they settle at a constant speed of terminal velocity  $v_t$ , and the deposition rate on the wall follows a linear law as derived from Stokes' law. For particles with a medium  $St$ , they tend to cluster into band-like structures, and these structures are found to align with the vertical movement of plumes in thermal turbulence (Park, O'Keefe & Richter 2018). To predict the deposition rate for medium  $St$ , Patočka, Calzavarini & Tosi (2020) and Patočka, Tosi & Calzavarini (2022) developed a mathematical model that describes particle sedimentation as a stochastic process. Particles move from areas of intense convection to lower-velocity regions near the horizontal boundaries of the cell, with the possibility of escaping low-velocity regions without settling. In addition, the effects of thermal and mechanical coupling on the turbulence structure of the LSC and boundary layers, as well as particles' motion, have received wide interest recently through simulations of two-way coupling (Oresta & Prosperetti 2013; Park *et al.* 2018) or four-way coupling (Demou *et al.* 2022) between the fluid and particles. Recent progress includes the works of Du & Yang (2022), Yang *et al.* (2022a,b), Sun, Wan & Sun (2024) and Chen & Prosperetti (2024), which incorporate thermal conduction and radiation, accounting for the thermal backreaction on the flow and examining its implications for heat transfer efficiency and flow structure modulation.

In addressing the complexities of natural and engineering fluid systems, such as atmospheric convection, oceanic currents and indoor air ventilation, it is crucial to examine the interactions between vertical buoyancy and the horizontal shear force (Hori *et al.* 2023). For example, Blass *et al.* (2020, 2021) incorporated a Couette-type shear into the RB system, where the top and bottom walls move in opposite directions at a constant speed. They found a transition in the flow dynamics from buoyancy-dominated to shear-dominated regimes as the strength of wall shear increased. In the buoyancy-dominated regime, the flow structure resembles canonical RB convection. In the shear-dominated regime, they observed the development of large meandering rolls. Yerragolam *et al.* (2022) then analysed the spectra of convective flux and turbulent kinetic energy, thereby offering insights into the small-scale flow structures within the same convection cell. Further, Jin *et al.* (2022) reported enhanced interactions between the LSC and secondary flows over rough shearing surfaces, leading to an increased generation of thermal plumes. Xu, Xu & Xi (2023) manipulated the movement of adiabatic sidewalls, thereby inducing vertical fluid motion that enhances heat transfer efficiency and can cause turbulent flows to relaminarize. In double diffusive convection, Li & Yang (2022) observed that even weak shear significantly alters the fingering morphology and transport properties of the system. Although recent advancements have shed light on the dynamics of single-phase and wall-sheared thermal turbulence, the complex interactions between a dispersed particulate phase and its surrounding fluid in wall-sheared thermal convection remain largely unexplored.

In this work, we aim to investigate particle transport and deposition behaviour within thermal turbulence under the influence of wall shearing. Motivated by studies of sand grains and pollutants dispersed in the air, we have chosen particles that are micrometres in size and much heavier than the surrounding fluid. Existing studies on particle-laden RB turbulence have largely focused on particles circulating within the LSC; here, we additionally consider scenarios where the flow structure changes under the influence of horizontal shear forces. The rest of this paper is organized as follows. In § 2, we present numerical details for the direct numerical simulation (DNS) of wall-sheared thermal turbulence laden with point particles. In § 3, we analyse the particles' transport behaviour in the cell and their spatial distribution, followed by their deposition patterns and a mathematical model to describe particle deposition rates. In § 4, the main findings of the present work are summarized.

## 2. Numerical methods

### 2.1. Problem statement

We explore the dynamics of particles within a two-dimensional (2-D) convection cell of dimensions  $L \times H$  (see figure 1a) and within a three-dimensional (3-D) convection cell of dimensions  $L \times H \times W$  (see figure 1b). Here,  $L$  is the length,  $H$  is the height and  $W$  is the width of the simulation domain,  $x$  represents the wall-shear direction,  $y$  represents the wall-normal direction and  $z$  represents the spanwise direction. The top and bottom walls of the cell are maintained at constant temperatures of  $T_{cold}$  and  $T_{hot}$ , respectively, while they move in opposite directions at a constant speed of  $u_w$ . The cell's vertical walls are configured to be periodic. Our simulation protocol is as follows: we start the simulation of single-phase turbulent thermal convection, and particles are introduced into the turbulence once the flow reaches a statistically stationary state. Initially, the cell contains  $N_0$  uniformly distributed stationary particles. We then advance the fluid flow and particle motion simultaneously, collecting statistics. We assume that particles adhere to

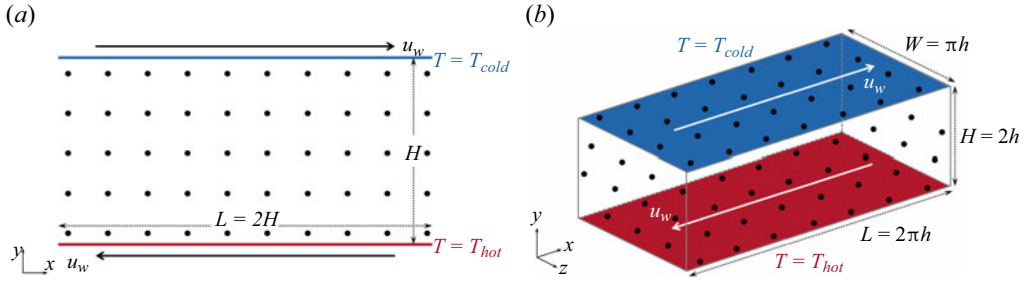


Figure 1. Schematic illustration of the wall-sheared convection cell and particles' initial positions for: (a) the 2-D simulations; (b) the 3-D simulations.

the wall upon contact, ceasing further movement within the convection cell and no longer interacting with other deposited particles.

### 2.2. Direct numerical simulation of thermal turbulence

In incompressible thermal convection, we employ the Boussinesq approximation to account for the temperature as an active scalar influencing the velocity field via buoyancy effects, under the assumption of constant transport coefficients. The equations governing fluid flow and the heat transfer process can be written as

$$\nabla \cdot \mathbf{u}_f = 0 \tag{2.1}$$

$$\frac{\partial \mathbf{u}_f}{\partial t} + \mathbf{u}_f \cdot \nabla \mathbf{u}_f = -\frac{1}{\rho_0} \nabla P + \nu \nabla^2 \mathbf{u}_f + g\beta(T_f - T_0)\hat{\mathbf{y}} \tag{2.2}$$

$$\frac{\partial T_f}{\partial t} + \mathbf{u}_f \cdot \nabla T_f = \alpha \nabla^2 T_f. \tag{2.3}$$

Here,  $\mathbf{u}_f$  is the fluid velocity, and  $P$  and  $T_f$  are the pressure and temperature of the fluid, respectively. The coefficients  $\beta$ ,  $\nu$  and  $\alpha$  denote the thermal expansion coefficient, kinematic viscosity and thermal diffusivity, respectively. Reference state variables are indicated by subscript zeros. Also,  $g$  represents gravitational acceleration, and  $\hat{\mathbf{y}}$  denotes the unit vector parallel to gravity in the wall-normal direction.

Introducing the non-dimensional variables

$$\left. \begin{aligned} \mathbf{x}^* &= \mathbf{x}/H, & t^* &= t/\sqrt{H/(g\beta\Delta T)}, & \mathbf{u}_f^* &= \mathbf{u}_f/\sqrt{g\beta\Delta TH}, \\ P^* &= P/(\rho_0 g\beta\Delta TH), & T_f^* &= (T_f - T_0)/\Delta T, \end{aligned} \right\} \tag{2.4}$$

we can rewrite (2.1)–(2.3) in a dimensionless form as

$$\nabla \cdot \mathbf{u}_f^* = 0 \tag{2.5}$$

$$\frac{\partial \mathbf{u}_f^*}{\partial t^*} + \mathbf{u}_f^* \cdot \nabla \mathbf{u}_f^* = -\nabla P^* + \sqrt{\frac{Pr}{Ra}} \nabla^2 \mathbf{u}_f^* + T_f^* \hat{\mathbf{y}} \tag{2.6}$$

$$\frac{\partial T_f^*}{\partial t^*} + \mathbf{u}_f^* \cdot \nabla T_f^* = \sqrt{\frac{1}{PrRa}} \nabla^2 T_f^*. \tag{2.7}$$

Here,  $H$  denotes the cell height and  $\Delta_T$  the temperature difference between the heating and cooling walls. The Rayleigh number ( $Ra$ ) and the Prandtl number ( $Pr$ ) are defined as

$$Ra = \frac{g\beta\Delta_T H^3}{\nu_f \alpha}, \quad Pr = \frac{\nu_f}{\alpha}. \quad (2.8a,b)$$

When an external wall shear is introduced, an additional control parameter, the wall-shear Reynolds number ( $Re_w = Hu_w/\nu$ ), is needed. The competition between buoyancy and shear effects can be quantified by the bulk Richardson number as  $Ri = Ra/(Re_w^2 Pr)$  (Blass *et al.* 2020, 2021; Yerragolam *et al.* 2022).

We adopt the spectral element method implemented in the open-source Nek5000 solver (version v19.0) for our DNS. Further details on the spectral element method and the validation of the Nek5000 solver are available in Fischer (1997) and Kooij *et al.* (2018). Previously, we verified the Nek5000 simulation results for wall-sheared thermal convection against those from an in-house GPU solver based on the lattice Boltzmann method (Xu, Shi & Zhao 2017; Xu & Li 2023). The results from both the Nek5000 solver and our lattice Boltzmann solver demonstrated consistent results for wall-sheared thermal convection (Xu *et al.* 2023).

### 2.3. Kinematics of the particles

We consider particles that are small enough not to influence the turbulence structure. The forces acting on a particle include the gravitational force  $F_{gravity}$  and the drag force  $F_{drag}$ . The gravitational force  $F_{gravity}$  points in the direction of gravitational acceleration, counteracted by buoyancy acting in the opposite direction, which is given as

$$F_{gravity} = \rho_p V_p \mathbf{g} - \rho_f V_p \mathbf{g}, \quad (2.9)$$

where  $\rho_p$  and  $V_p$  denote the particles' density and volume, respectively. The drag force  $F_{drag}$  results from the particles' effort to match the velocity of surrounding fluid, and is given as

$$F_{drag} = \frac{m_p}{\tau_p} (\mathbf{u}_f - \mathbf{u}_p) f(Re_p). \quad (2.10)$$

Here,  $\mathbf{u}_f$  is the fluid velocity at the particle's location, which is obtained by interpolating the fluid velocity fields from the mesh to the particle locations. The parameters  $m_p$  and  $\mathbf{u}_p$  represent the mass and velocity of the particle, respectively. The particle response time is  $\tau_p = \rho_p d_p^2 / (18\mu_f)$ , where  $d_p$  is the particle diameter. The drag correction factor  $f(Re_p)$  is a function of the particle Reynolds number  $Re_p = d_p |\mathbf{u}_f - \mathbf{u}_p| / \nu_f$ . We determined  $f(Re_p)$  in our simulations by dynamically calculating  $Re_p$  for each particle and then applying the correction factor based on the formula  $f(Re_p) = 1 + 0.15 Re_p^{0.687}$  (Clift, Grace & Weber 1978). In cases where  $Re_p \ll 1$ , we have  $f(Re_p) \approx 1$ , indicating the validity of Stokes' drag law. In this work, the 2-D cases can be approximated as a cross-section of the convection cell. Similar to Yang *et al.* (2022a,b), we assume the fluid layer has a finite but very thin thickness  $d_p$  in the spanwise direction. Both the fluid and particle motions are restricted in the spanwise direction, preventing movement along this axis. This restriction reduces the degrees of freedom, simplifying the dynamics. Consequently, while the overall flow is predominantly two-dimensional, the particles experience a 3-D environment due to the finite thickness of the fluid layer. The same formulation for the particle response time has been used by Patočka *et al.* (2020) and Yang *et al.* (2022a,b) in their 2-D studies.

The particle motion is then described by (van der Hoef *et al.* 2008; Maxey 2017)

$$\frac{d\mathbf{x}_p(t)}{dt} = \mathbf{u}_p(t) \quad (2.11)$$

$$\frac{d\mathbf{u}_p(t)}{dt} = \frac{\rho_p - \rho_f}{\rho_p} \mathbf{g} + \frac{\mathbf{u}_f(t) - \mathbf{u}_p(t)}{\tau_p} f(Re_p). \quad (2.12)$$

Here,  $\mathbf{x}_p$  denotes the position of the particle. For simplicity, we only consider the translational motion of isotropic spherical particles. To capture the anisotropic behaviour of particles in turbulent flows, the orientation and rotation dynamics of inertial particles can be modelled as described by Challabotla, Zhao & Andersson (2015) and Calzavarini, Jiang & Sun (2020). After non-dimensionalizing with the scales introduced above, we obtain

$$\frac{d\mathbf{x}_p^*}{dt^*} = \mathbf{u}_p^* \quad (2.13)$$

$$\frac{d\mathbf{u}_p^*}{dt^*} = -\Lambda \hat{\mathbf{y}} + \frac{\mathbf{u}_f^* - \mathbf{u}_p^*}{St_f} f(Re_p^*). \quad (2.14)$$

Here,  $\Lambda = (\rho_p - \rho_f)/(\rho_p \beta \Delta T)$  denotes the buoyancy ratio, which describes the relative importance of particle buoyancy with respect to thermal buoyancy of the fluid and  $St_f = \tau_p/t_f$  denotes the particle Stokes number, which describes the particle response time  $\tau_p$  relative to the flow time scale quantified by the free-fall time  $t_f = \sqrt{H/(g\beta\Delta T)}$ . At small Stokes numbers, the particle response time  $\tau_p$  is very small, making the term  $f(Re_p)(\mathbf{u}_f - \mathbf{u}_p)/\tau_p$  large unless  $\mathbf{u}_p$  is very close to  $\mathbf{u}_f$ . As a result, the particle velocity  $\mathbf{u}_p$  quickly matches the fluid velocity  $\mathbf{u}_f$ . In this regime, the drag force term dominates the particles' motion, and gravitational effects are minimal as particles follow the fluid flow. At large Stokes numbers, the particle response time  $\tau_p$  is large, causing the term  $f(Re_p)(\mathbf{u}_f - \mathbf{u}_p)/\tau_p$  to become small. Hence, the drag force term is negligible, and the particle motion is dominated by the gravitational term  $(\rho_p - \rho_f)\mathbf{g}/\rho_p$ . In this regime, particles sediment with a velocity that increases linearly over time as the effect of gravity becomes more significant.

To solve the above differential equations that describe the Lagrangian particle motion, we adopt a particle-in-cell (PIC) library implemented in ppiclF (Zwick 2019). The PIC library, ppiclF, is integrated into Nek5000 by establishing a communication and data exchange interface between the two codes. This process involves initializing the particle system within the Nek5000 framework and ensuring effective communication between the fluid solver and the particle solver. Each particle's position and velocity are integrated separately. To compute the fluid velocities at particle locations, the library uses spectral polynomial interpolation. This involves mapping Gauss–Lobatto–Legendre points within each spectral elements and evaluating barycentric Lagrange polynomials at the particles' coordinates, enhancing both accuracy and computational efficiency.

For particles settling in a stationary fluid where  $\mathbf{u}_f = 0$ , at terminal settling velocity  $\mathbf{u}_p(t) = \mathbf{u}_t$ , the particle's acceleration is zero (i.e.  $d\mathbf{u}_p/dt = 0$ ). The speed of terminal velocity  $v_t$  is then given by

$$v_t = \frac{d_p^2(\rho_p - \rho_f)g}{18\mu_f} \frac{1}{f(Re_p)}. \quad (2.15)$$

Parameter	Value
Rayleigh number ( $Ra$ )	$10^7, 10^8, 10^9$
Prandtl number ( $Pr$ )	0.71
Reference temperature ( $T_0$ )	300 K
Reference fluid density ( $\rho_0$ )	1.18 kg m <sup>3</sup>
Thermal expansion coefficient ( $\beta$ )	$3.36 \times 10^{-3} \text{ K}^{-1}$
Kinematic viscosity ( $\nu_f$ )	$1.57 \times 10^{-5} \text{ m}^2 \text{ s}^{-1}$
Thermal diffusivity ( $\alpha_f$ )	$2.22 \times 10^{-5} \text{ m}^2 \text{ s}^{-1}$
Temperature differences ( $\Delta_T$ )	5 K
Cell height ( $H$ )	0.28 m, 0.60 m, 1.28 m

Table 1. Simulation parameters and the corresponding fluid properties.

Due to the nonlinear relationship  $f(Re_p(v_t)) = 1 + 0.15(d_p v_t / \nu_f)^{0.687}$ , we cannot obtain an analytical solution directly. Instead, we use iterative methods to solve for  $v_t$  from the above equation.

#### 2.4. Simulation settings

We present 2-D simulation results in the cell with  $L = 2H$  for Rayleigh numbers in the range of  $10^7 \leq Ra \leq 10^9$  and a fixed Prandtl number of  $Pr = 0.71$  (motivated by the studies of sand grains and pollutants dispersed in the air), while the wall-shear Reynolds number  $Re_w$  is in the range  $0 \leq Re_w \leq 12\,000$ . To demonstrate the relevance of our results for 3-D wall-sheared thermal convection, we conducted a set of 3-D simulations in a cell with dimensions  $L \times H \times W = 2\pi h \times 2h \times \pi h$  at  $Ra = 10^7$  and  $Pr = 0.71$ . Here,  $h = H/2$  is the half-height of the cell. The wall-shear Reynolds number for the 3-D simulations is in the range  $0 \leq Re_w \leq 4000$ . Recently, Jie *et al.* (2022), Motoori, Wong & Goto (2022), Gao, Samtaney & Richter (2023) and Zhang, Cui & Zheng (2023) found that this domain size can accurately capture particle behaviours. The properties of air at a reference temperature of 300 K, including density, thermal expansion coefficient and kinematic viscosity, are listed in table 1. Additionally, we provide the height of the convection cell for a temperature difference of 5 K.

In the Nek5000 solver, the effective grid number is determined by the product of the number of spectral elements and the polynomial order. For the 2-D simulations, the cases with  $Ra = 10^7$  and  $10^8$  use uniform grids, while the cases with  $Ra = 10^9$  use non-uniform grids. For the 3-D simulations, the  $Ra = 10^7$  cases also use non-uniform grids. Specifically, the mesh spacing in the wall-parallel directions remains uniform for all cases; in the wall-normal direction, we adopt a cosine stretching function  $y(\xi) = -\cos[\pi(\xi + 1)/2]$  with  $\xi \in [-1, 1]$  to cluster points (Bernardini, Pirozzoli & Orlandi 2014). To validate the resolution, grid spacing in the wall-normal direction  $\Delta_y$  and time interval  $\Delta_t$  are compared against the Kolmogorov and Batchelor scales. The Kolmogorov length scale is estimated by the global criterion  $\eta_K = (\nu_f^3 / \langle \varepsilon_u \rangle_{V,t})^{1/4}$ , the Batchelor length scale is estimated by  $\eta_B = \eta_K Pr^{-1/2}$  (Batchelor 1959; Silano, Sreenivasan & Verzicco 2010) and the Kolmogorov time scale is estimated by  $\tau_{\eta_K} = \sqrt{\nu_f / \langle \varepsilon_u \rangle_{V,t}}$ . Here,  $\varepsilon_u$  denotes the turbulent kinetic energy dissipation rates, and  $\langle \dots \rangle_{V,t}$  denotes the volume- and time-averaged values. As shown in table 2, the grid spacing in the wall-normal direction meets the criterion  $\max(\Delta_y / \eta_K, \Delta_y / \eta_B) \approx 1$ , ensuring sufficient spatial resolution.

$Ra$	$Re_w$	$Ri$	Effective grid number	$(\Delta_y)_{max}/\eta_K$	$(\Delta_y)_{max}/\eta_B$	$(\Delta_t)_{max}/\tau_{\eta_K}$	$\eta_K$ (mm)
$10^7$ (2-D)	0	$\infty$	$369 \times 198$	0.62	0.52	0.0022	3.4
	500	56.34	$369 \times 198$	0.62	0.52	0.0019	3.4
	1000	14.08	$369 \times 198$	0.66	0.56	0.0024	3.2
	1500	6.26	$369 \times 198$	0.74	0.63	0.0024	2.8
	2000	3.52	$369 \times 198$	—	—	—	—
$10^8$ (2-D)	0	$\infty$	$792 \times 396$	0.83	0.70	0.0020	2.7
	1000	140.85	$792 \times 396$	0.96	0.81	0.0027	2.3
	2000	35.21	$792 \times 396$	0.97	0.82	0.0025	2.3
	3000	15.65	$792 \times 396$	0.97	0.82	0.0024	2.3
	4000	8.80	$792 \times 396$	0.97	0.82	0.0026	2.3
	5000	5.63	$792 \times 396$	0.91	0.76	0.0022	2.5
	6000	3.91	$1008 \times 504$	0.59	0.49	0.0010	3.0
	7000	2.87	$1008 \times 504$	0.55	0.47	0.0009	3.2
	8000	2.20	$1008 \times 504$	—	—	—	—
$10^9$ (2-D)	0	$\infty$	$1584 \times 792$	1.01	0.85	0.0013	2.4
	1000	1408.45	$1584 \times 792$	1.00	0.84	0.0013	2.4
	2000	352.11	$1584 \times 792$	1.01	0.85	0.0012	2.4
	3000	156.49	$1584 \times 792$	0.99	0.84	0.0012	2.4
	4000	88.03	$1584 \times 792$	1.01	0.85	0.0011	2.4
	5000	56.34	$1584 \times 792$	1.01	0.85	0.0013	2.4
	6000	39.12	$1584 \times 792$	0.95	0.80	0.0011	2.5
	9000	17.39	$1890 \times 945$	1.23	1.03	0.0018	2.6
	12 000	9.78	$1890 \times 1188$	0.87	0.73	0.0007	2.9
$10^7$ (3-D)	0	$\infty$	$144 \times 256 \times 128$	1.10	0.93	0.0054	2.2
	2000	3.52	$144 \times 256 \times 128$	1.15	0.97	0.0073	2.1
	4000	0.88	$144 \times 256 \times 128$	1.22	1.04	0.0068	2.0

Table 2. An *a posteriori* check of spatial and temporal resolutions of the simulations. The columns from left to right indicate the following: Rayleigh number  $Ra$ , wall-shear Reynolds number  $Re_w$ , Richardson number  $Ri$ , the effective grid number (i.e. the product of spectral element number and polynomial order), the ratio of the maximum grid spacing in the wall-normal direction over the Kolmogorov length scale, the ratio of the maximum grid spacing in the wall-normal direction over the Batchelor length scale, the ratio of the maximum time interval over the Kolmogorov time scale and the Kolmogorov length scale. Note that for the 2-D simulations at  $Ra = 10^7$  with  $Re_w = 2000$ , and at  $Ra = 10^8$  with  $Re_w = 8000$ , the flow is in the laminar state.

Additionally, the time intervals satisfy  $\max(\Delta_t/\tau_{\eta_K}) \approx 0.007$ , guaranteeing adequate temporal resolution.

We have varied both the diameter and the density of the particles in our simulations. Specifically, we explored the parameter space of  $5 \mu\text{m} \leq d_p \leq 80 \mu\text{m}$  and  $600 \text{ kg m}^{-3} \leq \rho_p \leq 3000 \text{ kg m}^{-3}$ . Initially, the 2-D cell contains  $N_0 = 100 \times 50 = 5000$  particles, and the 3-D cell contains  $N_0 = 150 \times 50 \times 75 = 562\,500$  particles. Motivated by studies of sand grains and pollutants dispersed in the air ( $\rho_p/\rho_f \gg 1$ ), we have the buoyancy ratio  $\Lambda \approx 1/(\beta\Delta_T)$  for all the simulation cases. In our simulations, we fixed the temperature difference  $\Delta_T = 5 \text{ K}$ , leading to  $\Lambda \approx 59.5$ . Then, (2.14) implies that we have one non-dimensional parameter, the Stokes number, to control the particle dynamics. The Stokes number based on the free-fall time scale is defined as  $St_f = \tau_p/t_f = \rho_p d_p^2 / (18\mu_f) / \sqrt{H/(g\beta\Delta_T)}$ , and  $St_f$  characterizes the large-scale effects. On the other



hand, the Stokes number based on the Kolmogorov time scale is defined as  $St_K = \tau_p / \tau_{\eta_K} = \rho_p d_p^2 / (18\mu_f) / \sqrt{\nu_f / \langle \varepsilon_u \rangle_{v,t}}$ , and  $St_K$  characterizes the small-scale effects. For clarity in the following discussion,  $St$  will denote  $St_K$  to reflect the particle inertia relative to that of small-scale fluid motion unless otherwise mentioned. We will use particle density  $\rho_p$  and particle diameter  $d_p$  to distinguish between different simulation cases. Dimensional numerical values for various particle quantities of interest in terms of  $St_f$  and  $St_K$  are tabulated in the supplementary table available at <https://doi.org/10.1017/jfm.2024.936>. In addition, we estimate the Kolmogorov length scale as  $\eta_K \geq 2.0$  mm (see table 2), which is around 25 times larger than the largest particle. The largest particle volume fraction of all cases is  $\phi \sim O(10^{-5})$ , thus justifying the use of a one-way coupling approach to model the motion of point particles in this work. Even for large  $St$ , where sedimentation dominates over convective or shear motions, the back reaction of particles on the fluid is generally less significant if  $\eta_K/d_p \gtrsim 10$  (Gore & Crowe 1989). In Appendix A, we further examine the spatial distribution of the time-averaged local Kolmogorov length scale to support that the point-particle model can be safely used. However, we acknowledge that this simplification holds primarily in dilute regimes (Balachandar & Eaton 2010); in more concentrated suspensions, the back reaction can become important and should be considered.

### 3. Results and discussion

#### 3.1. Particle transport in the convection cell

In figure 2, we show snapshots of temperature fields at various wall-shear Reynolds numbers  $Re_w$  from 2-D simulations, and the corresponding movie can be viewed in supplementary movie 1. These snapshots are taken when half of the total particles remain suspended in the convection cell. The canonical RB convection (see figure 2a–c) consists of two large-scale rolls rotating in opposite directions. At lower  $Re_w$  (see figure 2d–f), the horizontal wall-shear effects are weak, and the dominant flow patterns are similar to those in the canonical RB convection. As the wall shear increases, the large-scale rolls undergo horizontal expansion, eventually leading to a transition into the zonal flow state (see figure 2g–i). Zonal flows are primarily horizontal flows typically aligned with the rotation axis in rotating systems (Goluskin *et al.* 2014; Zhang *et al.* 2020; Lin & Jackson 2021) or along a specific direction in non-rotating systems (Wang *et al.* 2020b; Winchester, Dallas & Howell 2021; Jin *et al.* 2022). These flows exhibit large-scale, coherent structures that can span the entire system and are often associated with banded structures in the flow field. Previous 2-D studies on zonal flow were primarily conducted in convection cells with free-slip boundaries, which do not exert shear stress to slow down the fluid, and the periodicity of the flow system allows for a horizontal mean flow (Goluskin *et al.* 2014; Wang *et al.* 2020b; Winchester *et al.* 2021). In contrast, our work shows that moving boundaries induce a horizontal mean flow, forming the zonal flow. The overall trend in the 2-D flow pattern is similar to that in convection cells with rough shearing walls (Jin *et al.* 2022).

Regarding particle movement, the combined effects of particle diameter and particle density are reflected in the dimensionless Stokes number. For clarity of presentation, most results in this paper are shown at a fixed particle density but with varying particle diameters to present small, medium and large Stokes number cases. Particles with small  $St$  (see figure 2a,d,g) are randomly distributed throughout the convection cell. These particles quickly adapt to changes in the surrounding flow, with little to no agglomeration. For medium  $St$  (see figure 2b,e,h), we observe a greater concentration

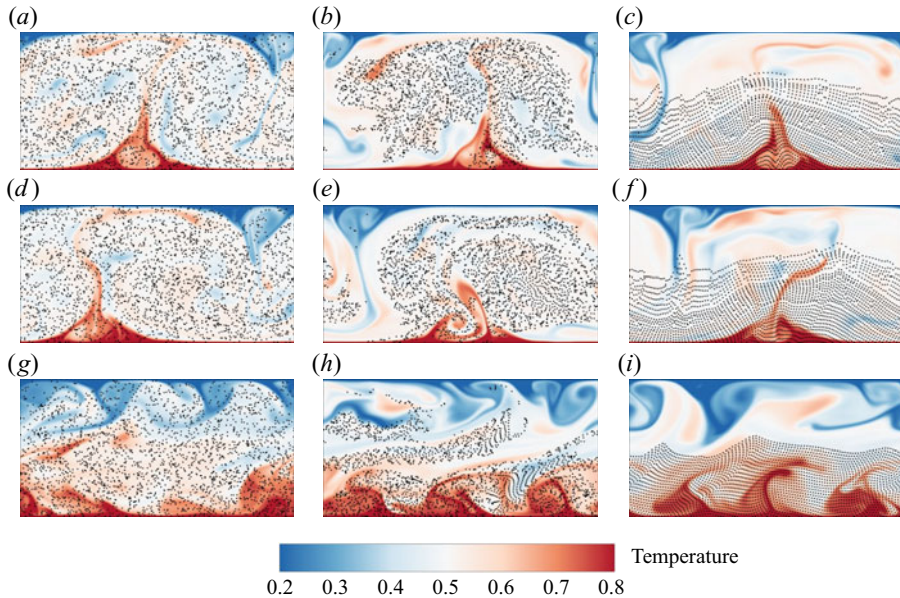


Figure 2. Typical instantaneous temperature fields (contours) and particle positions (black dots, sizes artificially increased for better flow visualization) from 2-D simulations at (a–c)  $Re_w = 0$ , (d–f)  $Re_w = 2000$  and (g–i)  $Re_w = 6000$ , with  $Ra = 10^8$ . Particle density is fixed as  $\rho_p = 3000 \text{ kg m}^{-3}$ , with diameters of (a,d,g)  $d_p = 5 \mu\text{m}$ , (b,e,h)  $d_p = 20 \mu\text{m}$  and (c,f,i)  $d_p = 80 \mu\text{m}$ . Corresponding Stokes numbers are (a)  $St = 4.86 \times 10^{-4}$ , (b)  $St = 7.78 \times 10^{-3}$ , (c)  $St = 1.25 \times 10^{-1}$ , (d)  $St = 6.64 \times 10^{-4}$ , (e)  $St = 1.06 \times 10^{-2}$ , (f)  $St = 1.70 \times 10^{-1}$ , (g)  $St = 3.93 \times 10^{-4}$ , (h)  $St = 6.29 \times 10^{-3}$  and (i)  $St = 1.01 \times 10^{-1}$ .

of particles over upwelling areas, with downwelling regions displaying fewer particles. This counterintuitive observation aligns with our previous findings (Xu *et al.* 2020) and independent research by Patočka *et al.* (2020, 2022). The physical interpretation is that, for particles circulating within large-scale rolls in the convection cell, when they approach the bottom boundary beneath downwellings, they are likely to be carried by the fast-moving edges of the rolls toward regions beneath upwellings. In these upwelling regions, particles may enter areas with slower flow due to small-scale irregularities caused by new plume generation. These low-velocity regions increase the likelihood of particle sedimentation, leading to an accumulation of particles beneath the upwellings. In sheared convection cells, horizontal shear forces facilitate particle lateral dispersion, which is particularly apparent in figure 2(h). For large  $St$  (see figure 2c,f,i), the inertia of the particles is dominant, causing them to settle and become nearly unresponsive to the carrier flow, similar to behaviour observed in quiescent fluid environments. As we will demonstrate later, even these large  $St$  particles are slightly influenced by the turbulent flow.

In figure 3, we further show snapshots of the velocity component  $v$  at the channel centre plane and particle positions from 3-D simulations, and the corresponding movie can be viewed in supplementary movie 2. In thermal convection, rising fluids are warmer and falling fluids are colder. At  $Re_w = 0$  and  $Ra = 10^7$ , the flow structure resembles the canonical RB convection (Stevens *et al.* 2018). As  $Re_w$  increases to 2000, the flow enters a transitional regime where the interaction between the imposed shear and buoyancy becomes significant. Large, elongated thermal plumes start to transform into thin, straight, elongated streaks aligned in the streamwise direction. Eventually, streamwise-oriented rolls are formed at  $Re_w = 4000$  (Pirozzoli *et al.* 2017; Blass *et al.* 2020). To further

## Particle transport and deposition

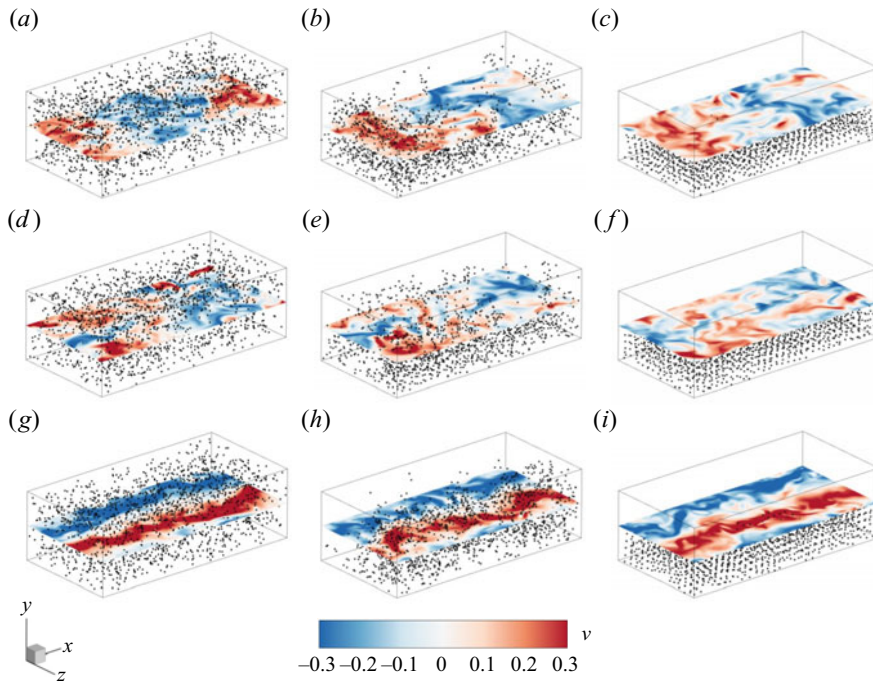


Figure 3. Typical instantaneous slice of velocity component  $v$  at the channel centre plane (contours) and particle positions (black dots, sizes artificially increased for better flow visualization, here 0.8% of suspended particles are shown for clarity) from 3-D simulations at (a–c)  $Re_w = 0$ , (d–f)  $Re_w = 2000$  and (g–i)  $Re_w = 4000$ , with  $Ra = 10^7$ . Particle density is fixed as  $\rho_p = 3000 \text{ kg m}^{-3}$ , with diameters of (a,d,g)  $d_p = 5 \text{ }\mu\text{m}$ , (b,e,h)  $d_p = 20 \text{ }\mu\text{m}$  and (c,f,i)  $d_p = 80 \text{ }\mu\text{m}$ . Corresponding Stokes numbers are (a)  $St = 7.05 \times 10^{-4}$ , (b)  $St = 1.13 \times 10^{-2}$ , (c)  $St = 1.80 \times 10^{-1}$ , (d)  $St = 7.70 \times 10^{-4}$ , (e)  $St = 1.23 \times 10^{-2}$ , (f)  $St = 1.97 \times 10^{-1}$ , (g)  $St = 8.83 \times 10^{-4}$ , (h)  $St = 1.41 \times 10^{-2}$  and (i)  $St = 2.26 \times 10^{-1}$ .

elucidate the nature of these large-scale rolls, we present time-averaged streamlines coloured by the vertical velocity  $v$ , as shown in figure 4(a–c). At  $Re_w = 0$ , the averaged streamlines show a well-defined roll structure aligned in the spanwise direction. As  $Re_w$  increases to 4000, the averaged streamlines transition to an organized pattern aligned with the streamwise direction. Additionally, we measure the velocity orientation  $\theta$ , defined as the angle between the projection of the velocity vector onto the  $x$ – $z$  plane and the positive  $x$ -axis. We calculate the probability density functions (p.d.f.s) of  $\theta$  for fluid nodes in the region  $0.1H \leq y \leq 0.9H$ , and present their time evolution in figure 4(d–f). At  $Re_w = 0$ , the p.d.f.s indicate high probability values consistently around  $0^\circ$  and  $180^\circ$ , suggesting that the roll axes are predominantly aligned in the spanwise direction, without exhibiting complex motions as seen in an RB cell with a larger length-to-width aspect ratio (Vogt *et al.* 2018; Li *et al.* 2022; Teimurazov *et al.* 2023). At  $Re_w = 4000$ , the p.d.f.s shift to show high probability values around  $\pm 90^\circ$ , indicating that the roll axes are consistently aligned in the streamwise direction.

We then examine the global response parameters of the Nusselt number ( $Nu$ ) and Reynolds number ( $Re$ ) on the control parameter  $Re_w$  in the 2-D flow system. Here, the heat transfer efficiency is calculated as  $Nu = 1 + \sqrt{PrRa} \langle v^* T^* \rangle_{V,t}$ , and the global flow strength of the convection is calculated as  $Re = \sqrt{\langle \|u\|^2 \rangle_{V,t}} H / \nu_f$ . Moreover, we consider

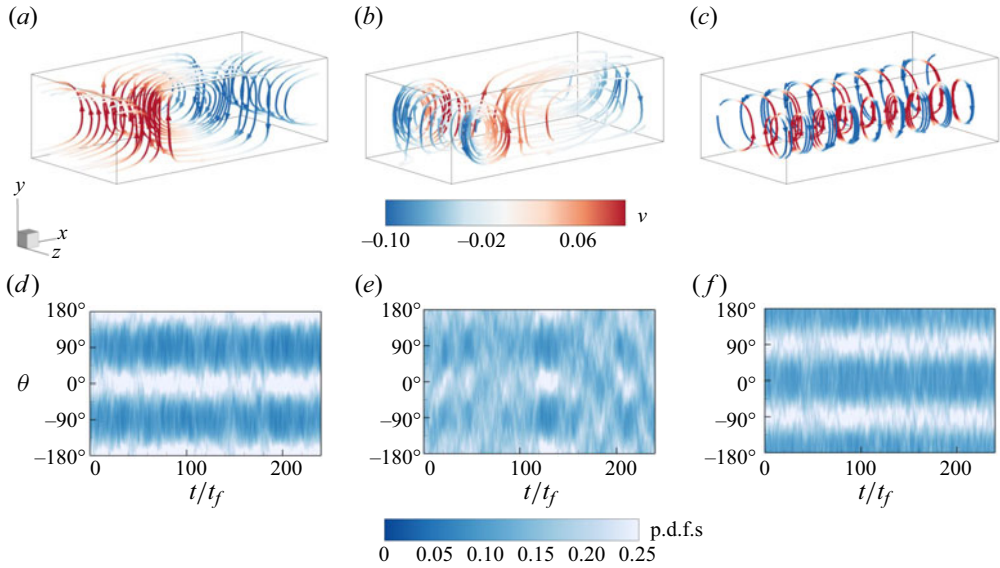


Figure 4. (a–c) Time-averaged streamlines coloured by the vertical velocity  $v$ , (d–f) time evolution of the p.d.f.s of the instantaneous velocity orientation  $\theta$  at (a,d)  $Re_w = 0$ , (b,e)  $Re_w = 2000$  and (c,f)  $Re_w = 4000$ , with  $Ra = 10^7$ .

the lateral and vertical components of  $Re$ , respectively, as  $Re_x = \sqrt{\langle u^2 \rangle_{V,t}} H / \nu_f$ ,  $Re_y = \sqrt{\langle v^2 \rangle_{V,t}} H / \nu_f$ . Both  $Nu$  and  $Re$  exhibit sharp changes and abrupt transitions at  $Re_w \simeq 1500$  with  $Ra = 10^7$  (see figure 5a,d), at  $Re_w \simeq 5000$  with  $Ra = 10^8$  (see figure 5b,e), suggesting a threshold for the competition between wall shear and buoyancy that leads to changes in the flow state from LSCs to zonal flows in 2-D simulations. The heat transport behaviour in wall-sheared thermal turbulence is governed by the interaction between the buoyancy-driven LSC and the shear introduced by the moving walls. At higher wall shear, strong wall instabilities disrupt the large-scale rolls, which are crucial for carrying thermal energy away from the wall and efficiently transporting heat. When these large-scale structures are disrupted, small-scale turbulent motions become more prevalent, and the convective motions near the wall increase. However, these motions become more localized and less effective in transporting heat across larger vertical distances, thus decreasing the overall efficiency of heat transport. Regarding the velocity fields, LSCs exhibit both significant vertical and horizontal velocity components, while zonal flows in two dimensions show strong horizontal velocities with a lower vertical component. At a fixed Rayleigh number, when the wall shear becomes sufficiently strong, the flow transitions to laminar Couette flow, causing the vertical flow velocity component to become nearly zero. For a Rayleigh number of  $10^7$ , this transition occurs approximately at  $Re_w \simeq 2000$  (see figure 5d); for a Rayleigh number of  $10^8$ , the transition happens at around  $Re_w \simeq 8000$  (see figure 5e). At an even higher Rayleigh number of  $10^9$ , based on the results of Jin *et al.* (2022) and Xu *et al.* (2023), we speculate that the transitions to laminar Couette flow occurs at a much larger  $Re_w$ , beyond the parameter range explored in the present work.

We quantitatively describe the influence of wall shear on particle motion by analysing the p.d.f.s of their velocity components ( $u_p$  and  $v_p$ ), as shown in figure 6. For particles with small and medium  $St$  (see figure 6a,b), the p.d.f.s of  $u_p$  are characterized by a single

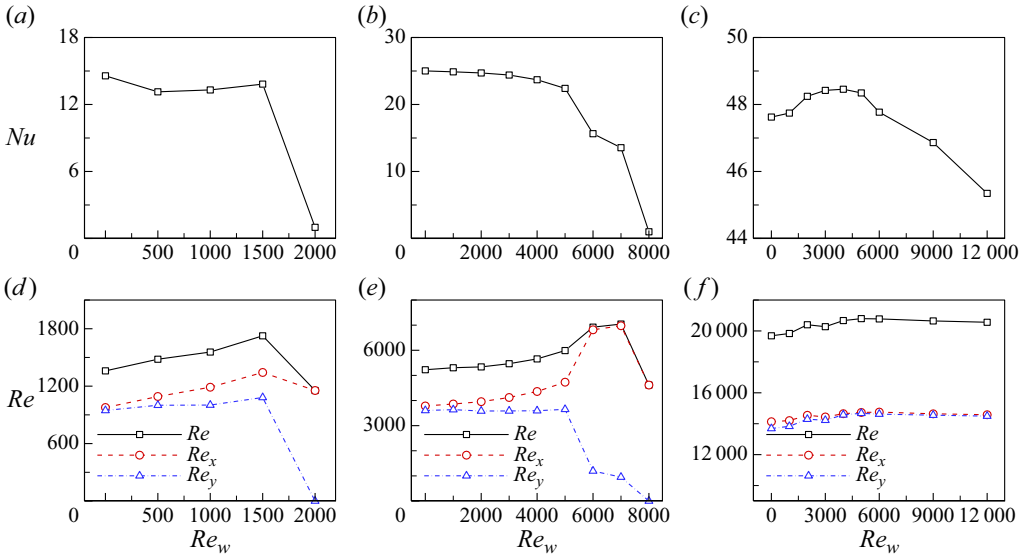


Figure 5. (a–c) Nusselt number and (d–f) Reynolds number as a function of  $Re_w$ : (a,d) with  $Ra = 10^7$ , (b,e) with  $Ra = 10^8$ , (c,f) with  $Ra = 10^9$ .

peak centred around zero, exhibiting symmetry for  $Re_w \lesssim 5000$ , suggesting a substantial likelihood of particles circulating within the LSC of convective flows. As  $Re_w$  increases to 6000, the p.d.f.s of  $u_p$  change to a bimodal distribution with two peaks off zero value, which can be attributed to the horizontal drift of particles caused by the wall shear. In addition, with increasing  $St$ , the peak corresponding to the negative  $u_p$  exceeds that of the positive, suggesting an increased likelihood for particle suspension in the lower domain of the cell due to sedimentation (note the bottom wall is moving in the negative  $x$ -direction). For large  $St$  (see figure 6c), we can deduce that these particles are still minorly influenced by the turbulent flow because they exhibit horizontal motions with finite positive or negative  $u_p$ . Regarding the p.d.f.s of  $v_p$ , for small and medium  $St$  (see figure 6d,e), their shapes are much narrower at  $Re_w = 6000$  compared with those at lower  $Re_w$ , indicating attenuated vertical motions in the zonal flow. This trend becomes more pronounced for large  $St$  (see figure 6f), where  $v_p$  values are predominantly negative. This implies vertical updrafts are insufficient to counter the gravitational settling, preventing these particles from rising with the flow currents.

We examine the p.d.f.s of the particle Reynolds number  $Re_p = d_p |\mathbf{u}_f - \mathbf{u}_p| / \nu_f$ , as shown in figure 7. We can see from figure 7(a,b) that, for particles with small  $St$ ,  $Re_p$  is generally less than  $10^{-3}$ ; for medium  $St$ ,  $Re_p$  is generally less than  $10^{-1}$ . In the presence of a pronounced LSC within the flow, the p.d.f.s of  $Re_p$  manifest dual peaks, corresponding to the particles ascending or descending with the LSC. As wall shear increases, the  $Re_p$  will also increase and exhibit enhanced intermittency. However, when  $Re_w$  further increases up to 6000,  $Re_p$  decreases and the p.d.f.s of  $Re_p$  change from a bimodal to unimodal distribution. This shift is attributed to the decreased vertical velocity component  $v_p$  of the particles within the convective flow, as evidenced by figure 6(d–f). For large  $St$ ,  $Re_p$  is as large as  $Re_p \sim O(1)$  and spans a more extensive range, as shown in figure 7(c), which emphasizes the necessity of incorporating a drag correction factor  $f(Re_p)$  into the drag force calculations. We further plot the p.d.f.s of normalized particle Reynolds number  $(Re_p - \mu_{Re_p}) / \sigma_{Re_p}$ , as shown in figure 7(d–f). For particles with small  $St$  (see figure 7d),

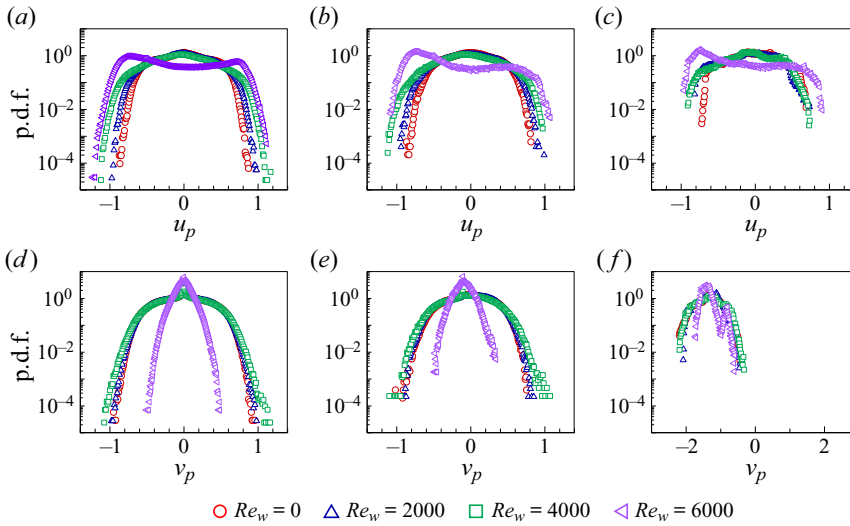


Figure 6. The p.d.f.s of the particle velocity component (*a–c*) in the horizontal direction ( $u_p$ ), and (*d–f*) in the vertical direction ( $v_p$ ) with  $Ra = 10^8$ . Particle density is fixed as  $\rho_p = 3000 \text{ kg m}^{-3}$ , with diameters of (*a,d*)  $d_p = 5 \text{ }\mu\text{m}$ , (*b,e*)  $d_p = 20 \text{ }\mu\text{m}$  and (*c,f*)  $d_p = 80 \text{ }\mu\text{m}$ .

the p.d.f.s of  $Re_p$  are close to the Gaussian distribution (denoted by the dashed line in the figure). However, with an increase in  $Re_w$ , the deviations in the tails of the p.d.f.s become more pronounced, indicating more intermittency events due to the influence of wall shear. For medium  $St$  (see figure 7*e*), the p.d.f.s generally follow the Gaussian distribution, although there appear to be deviations with heavier tails, which implies there are more instances of  $Re_p$  values deviating from the mean. For large  $St$  (see figure 7*f*), the p.d.f.s of  $Re_p$  are distinctly different from a Gaussian distribution, indicating a distinct distribution pattern where particle motion is nearly unaffected by the turbulence.

Previous studies have shown that, even in homogeneous isotropic turbulence, the particles may not distribute homogeneously but exhibit clustering behaviour (Wang & Maxey 1993; Bosse, Kleiser & Meiburg 2006; Calzavarini *et al.* 2008). To identify the clustering behaviour of particles during their transport in the wall-sheared convection cell, we employ a quantitative analysis using Voronoï diagrams (Monchaux, Bourgoin & Cartellier 2010, 2012). A Voronoï cell is defined as a collection of points closer to its corresponding particle than to any other; thus, the area (or volume) of a Voronoï cell inversely correlates with local particle concentration. In figure 8, we show Voronoï diagrams for the particle distribution, corresponding to the instantaneous state presented in figure 2. For particles with small  $St$  (see figure 8*a,d,g*), Voronoï cells are of similar size and relatively evenly distributed in space, indicating a low degree of aggregation. For medium  $St$  (see figure 8*b,e,h*), the areas of their Voronoï polygon exhibit much higher variability, indicating an increased level of spatial inhomogeneity. For large  $St$  (see figure 8*c,f,i*), large voids are formed at the upper part of the convection cell, containing few to no particles. This is because most particles settle down and do not circulate in the cell, as revealed by the predominantly negative  $v_p$  velocity components shown in figure 6(*f*).

We then analyse the statistical distribution of the Voronoï cell area  $A$ . Figure 9 shows the p.d.f.s of the normalized Voronoï cell area  $A/\langle A \rangle$ , corresponding to the instantaneous state presented in figure 8. Here,  $\langle A \rangle$  represents the mean value of  $A$  at the current moment. For particles with small  $St$  (see figure 9*a*), the Voronoï cells are randomly distributed

Particle transport and deposition

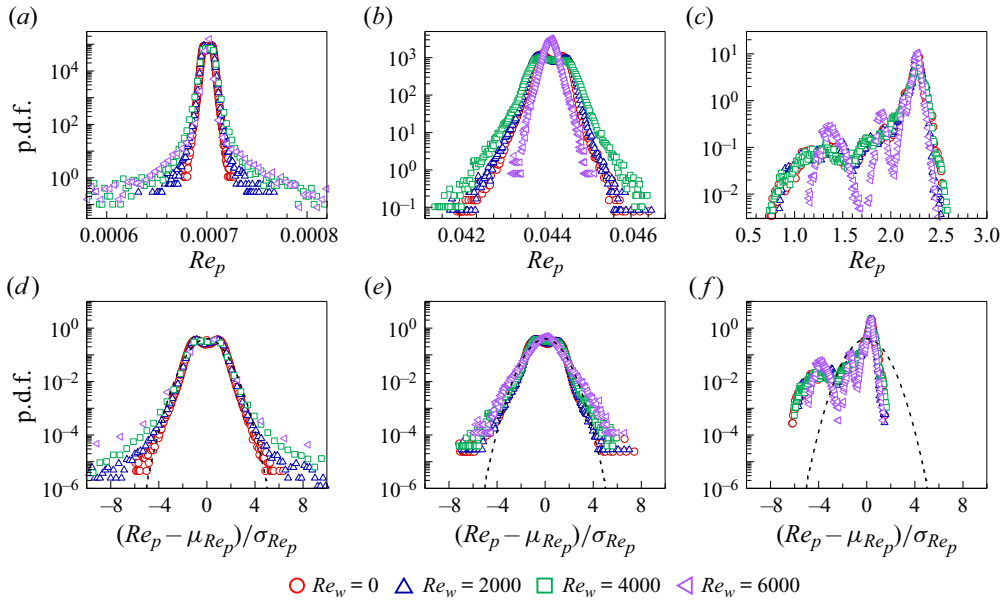


Figure 7. (a–c) The p.d.f.s of particle Reynolds number  $Re_p$  and (d–f) the p.d.f.s of normalized particle Reynolds number  $(Re_p - \mu_{Re_p})/\sigma_{Re_p}$  with  $Ra = 10^8$ . Particle density is fixed as  $\rho_p = 3000 \text{ kg m}^{-3}$ , with diameters of (a,d)  $d_p = 5 \mu\text{m}$ , (b,e)  $d_p = 20 \mu\text{m}$  and (c,f)  $d_p = 80 \mu\text{m}$ . Dashed lines in (d–f) represent the Gaussian distribution.

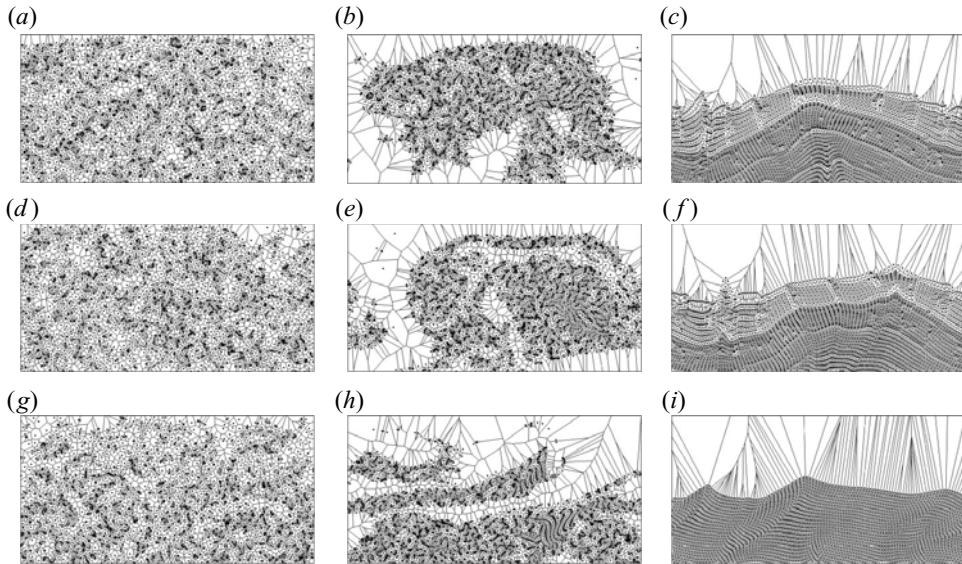


Figure 8. Typical instantaneous Voronoi diagrams for particles at (a–c)  $Re_w = 0$ , (d–f)  $Re_w = 2000$ , (g–i)  $Re_w = 6000$  with  $Ra = 10^8$ . Particle density is fixed as  $\rho_p = 3000 \text{ kg m}^{-3}$ , with diameters of (a,d,g)  $d_p = 5 \mu\text{m}$ , (b,e,h)  $d_p = 20 \mu\text{m}$  and (c,f,i)  $d_p = 80 \mu\text{m}$ .

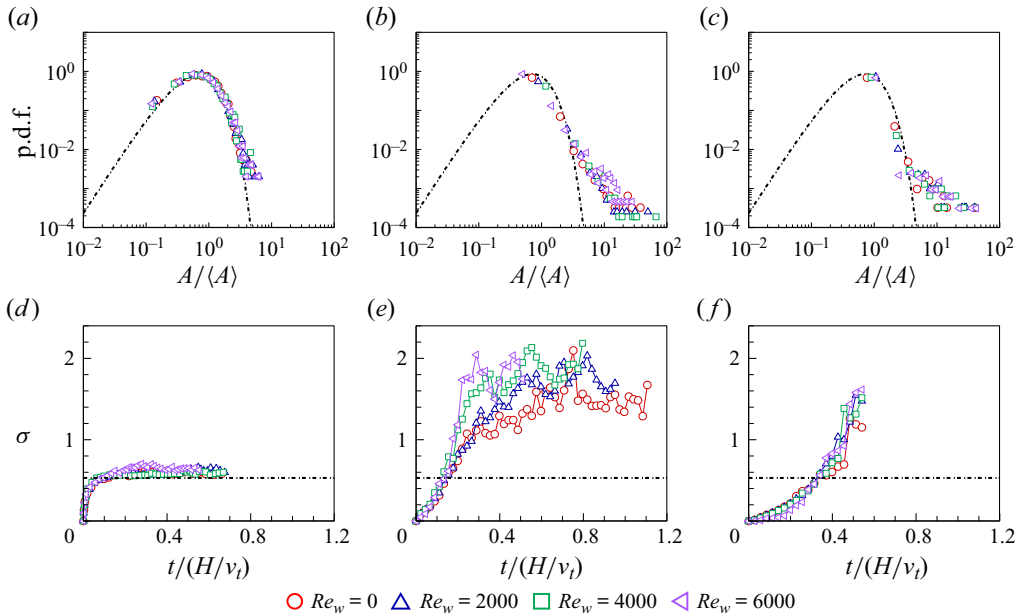


Figure 9. (a–c) The p.d.f.s of the normalized Voronoi cell area  $A/\langle A \rangle$  corresponding to the instantaneous state presented in figure 8, and (d–f) time evolution of the standard deviation of the normalized Voronoi cell area. Panels show (a,d)  $d_p = 5 \mu\text{m}$ , (b,e)  $d_p = 20 \mu\text{m}$  and (c,f)  $d_p = 80 \mu\text{m}$ .

throughout the flow field, and the distribution of their areas satisfies the  $\Gamma$  distribution (Ferenc & Néda 2007; Tagawa *et al.* 2012)

$$f_d(m) = \frac{[(3d + 1)/2]^{(3d+1)/2}}{\Gamma[(3d + 1)/2]} m^{(3d-1)/2} \exp\left(-\frac{3d + 1}{2} m\right), \quad m = \frac{A}{\langle A \rangle}, \quad (3.1)$$

where  $d = 2$  denotes the analysis in two dimensions. For medium  $St$  (see figure 9b), the p.d.f.s have a peak near unity, yet exhibit pronounced tails indicative of larger Voronoi cell areas, deviating from the  $\Gamma$  distribution. This deviation from the  $\Gamma$  distribution signals a departure from randomness, indicative of local preferential concentration. For large  $St$  (see figure 9c), the p.d.f.s exhibit more pronounced tails towards larger Voronoi cell areas, indicating intensified void formation.

Figure 9(d–f) further shows the time evolution of the standard deviation  $\sigma$  of the normalized Voronoi cell area, serving as an indicator of spatial inhomogeneity. Due to particle deposition on the wall and constantly reducing particle numbers, the particles statistics cannot reach a statistically stationary state. Here, we only plot the time series from the initial state to the time at which half of the total particles remain suspended in the convection cell. For particles with small  $St$  (see figure 9d), the standard deviation is the lowest, approaching the theoretical expectation for the  $\Gamma$  distribution (i.e.  $\sigma = 0.53$ , denoted by the dash-dotted line). For medium  $St$  (see figure 9e), the greatest clustering is observed as the standard deviation of their Voronoi area significantly exceeds 0.53. For large  $St$  (see figure 9f), the clustering also occurs; however, the influence of variations in wall-shear strength  $Re_w$  appears to be negligible in contrast to those with medium  $St$ .

Based on the above analysis, we arrive at the following mathematical model for the spatial distribution of particle concentration. We denote the initial concentration of particles as  $n_0 = N_0/(LHW)$ , where  $N_0$  is the initial number of particles laden in



the fluid. We define the instantaneous particle line density averaged over a horizontal cross-section as  $n(\tau, y) = N(\tau, y)/(LW)$  at a given time  $\tau$  and height  $y$ , where  $N(\tau, y)$  is the instantaneous particle number at time  $\tau$  and height  $y$ . We also define the time-averaged local particle concentration over a horizontal cross-section and along the cell height as  $\langle n(y) \rangle_t$ , where the average  $\langle \cdot \rangle_t$  is calculated over time  $t$ . In transient processes, the particle concentration changes over time, and the time-averaged concentration represents the overall behaviour of the particles during a specified time interval, which is crucial for understanding the long-term behaviour of the system, even when the process is not in a steady state.

For particles with small  $St$ , they are randomly distributed throughout the convection cell, and they exhibit an exponential decay rate as  $N(\tau) = N_0 \exp[-\tau/(H/v_t)]$  (Martin & Nokes 1989), with  $N(\tau)$  being the number of particles that remain laden in the convection cell at time  $\tau$ . Following the assumption of Martin & Nokes (1989), turbulent convection ensures that particles are mixed homogeneously across the flow, which leads to  $N(\tau, y) = N(\tau)/H$ , and particle concentration is uniform across the horizontal plane of the fluid. Thus, at a given time  $\tau$  and height  $y$ , the instantaneous particle line density  $n(\tau, y)$  is

$$n(\tau, y) = \frac{N(\tau, y)}{LW} = \frac{N(\tau)}{LHW} = \frac{N_0 \exp\left(-\frac{\tau}{H/v_t}\right)}{LHW} = n_0 \exp\left(-\frac{\tau}{H/v_t}\right). \quad (3.2)$$

Then, the horizontal- and time-averaged local particle concentration, which represents the number density of particles suspended in the convection cell over a given time period and horizontal cross-section, for small  $St$ , is

$$\frac{\langle n(y) \rangle_t}{n_0} = \frac{\left(\int_0^t n(\tau, y) \, d\tau\right) / t}{n_0} = -\frac{H}{v_t t} \left[ \exp\left(-\frac{t}{H/v_t}\right) - 1 \right]. \quad (3.3)$$

In the above,  $\langle n(y) \rangle_t$  is further normalized by initial concentration  $n_0$ .

For large  $St$ , sedimentation occurs almost independently of the carrier flow, analogous to settling behaviour of particles in quiescent fluid environments. Thus, we can ignore their lateral motion and simply assume they settle at a constant speed of terminal velocity  $v_t$ . From the initial state of uniform distribution, after a duration of  $\tau$ , the particle ensemble settles a vertical distance of  $v_t \tau$ . Thus, the instantaneous particle line density  $n(\tau, y)$  is

$$n(\tau, y) = \begin{cases} 0, & H - v_t \tau < y \leq H \\ n_0, & y \leq H - v_t \tau. \end{cases} \quad (3.4)$$

We consider at the time  $\tilde{t} \in [0, t]$  the instantaneous local particle concentration  $n(\tilde{t}, y)$  that decreases from  $n_0$  to 0 across a height interval  $\tilde{y}$ , where  $\tilde{y} \in [H - v_t \tilde{t}, H]$ , resulting in  $H - v_t \tilde{t} = \tilde{y}$ . Thus, the horizontal- and time-averaged local particle concentration (further normalized by  $n_0$ ), for large  $St$ , is

$$\frac{\langle n(y) \rangle_t}{n_0} = \frac{\left(\int_0^t n(\tau, y) \, d\tau\right) / t}{n_0} = \begin{cases} \frac{\left(\int_0^{\tilde{t}} n_0 \, d\tau\right) / t}{n_0} + \frac{\left(\int_{\tilde{t}}^t 0 \, d\tau\right) / t}{n_0}, & H - v_t t \leq y \leq H \\ \frac{\left(\int_0^t n_0 \, d\tau\right) / t}{n_0}, & y \leq H - v_t t. \end{cases} \quad (3.5)$$

The above equation can be further simplified to

$$\frac{\langle n(y) \rangle_t}{n_0} = \begin{cases} \frac{H-y}{v_t t}, & H - v_t t \leq y \leq H \\ 1, & y \leq H - v_t t. \end{cases} \quad (3.6)$$

We choose the time-average  $\langle \cdot \rangle_{t_{1/2}}$  from the initial state up to the state when half of the total particles deposit on the wall (a duration referred to as half-life time  $t_{1/2}$  from now on). For particles with small  $St$ , they exhibit an exponential deposition rate (Martin & Nokes 1989). The half-life time can be obtained by setting  $N_s/N_0 = 1 - \exp[-t_{1/2}/(H/v_t)] = 1/2$ , which further gives  $t_{1/2} = (H \ln 2)/v_t$ . Here,  $N_s$  is the number of particles that have settled and deposited on the wall. Substituting this time duration into (3.3), we derive the horizontal- and time-averaged local particle concentration for small  $St$  as

$$\frac{\langle n(y) \rangle_{t_{1/2}}}{n_0} = \frac{1}{2 \ln 2}. \quad (3.7)$$

For large  $St$ , the deposition rate on the wall follows a linear law as derived from Stokes' law. The half-life time can be obtained by setting  $N_s/N_0 = t_{1/2}/(H/v_t) = 1/2$ , which further gives  $t_{1/2} = 0.5H/v_t$ . Substituting this into (3.6), we derive the horizontal- and time-averaged local particle concentration for large  $St$  as

$$\frac{\langle n(y) \rangle_{t_{1/2}}}{n_0} = \begin{cases} 2 \left(1 - \frac{y}{H}\right), & 0.5H \leq y \leq H \\ 1, & y \leq 0.5H. \end{cases} \quad (3.8)$$

In figure 10, we compare the theoretical estimations of  $\langle n(y) \rangle_{t_{1/2}}/n_0$ , namely (3.7) and (3.8), with both 2-D and 3-D simulation results. For particles with small  $St$  (see figure 10a,d), the local particle concentration generally agrees with the theoretical predictions except for the discrepancy at  $y > 0.8H$ . This discrepancy may be attributed to the finite  $St$  effect (i.e. a small but not non-zero  $St$ ), which results in a reduced particle presence in the upper boundary layer. At  $Re_w = 6000$  in the 2-D simulations, the flow transitions from the LSC to zonal flow, thus the assumption of a spatially uniform particle concentration proposed by Martin & Nokes (1989) may no longer be valid, leading to significant deviation from (3.7). Specifically, when the LSC transitions to a zonal flow state, the updrafts are significantly weakened. This weakening results in fewer particles drifting upwards and more particles settling down, leading to a higher particle concentration at the bottom of the zonal flow compared with the LSC state. For medium  $St$  (see figure 10b,e), the absence of a corresponding model precludes a direct comparison; however, we provide a qualitative description of particle concentration. When the LSC is present, the local particle concentration appears to be consistent in the bulk region, but exhibits an increase with increasing  $Re_w$  in the bottom boundary layer, implying that wall shear accelerates particle sedimentation. At  $Re_w = 6000$  in the 2-D simulations, the changes in flow states lead to distinctly different profiles for the local particle concentration compared with those at lower  $Re_w$ . For large  $St$  (see figure 10c,f), the local particle concentration generally agrees with the theoretical prediction (3.8) across all  $Re_w$ , highlighting again that the particles' motion is nearly not affected by the turbulent flows of the carrier fluid (i.e. either LSC or zonal flow state). When the wall shear becomes sufficiently strong, the vertical flow velocity component weakens significantly. Since the settling velocity of particles is strongly influenced by the vertical flow velocity component, the settling velocity of particles then approaches that in a stationary flow field

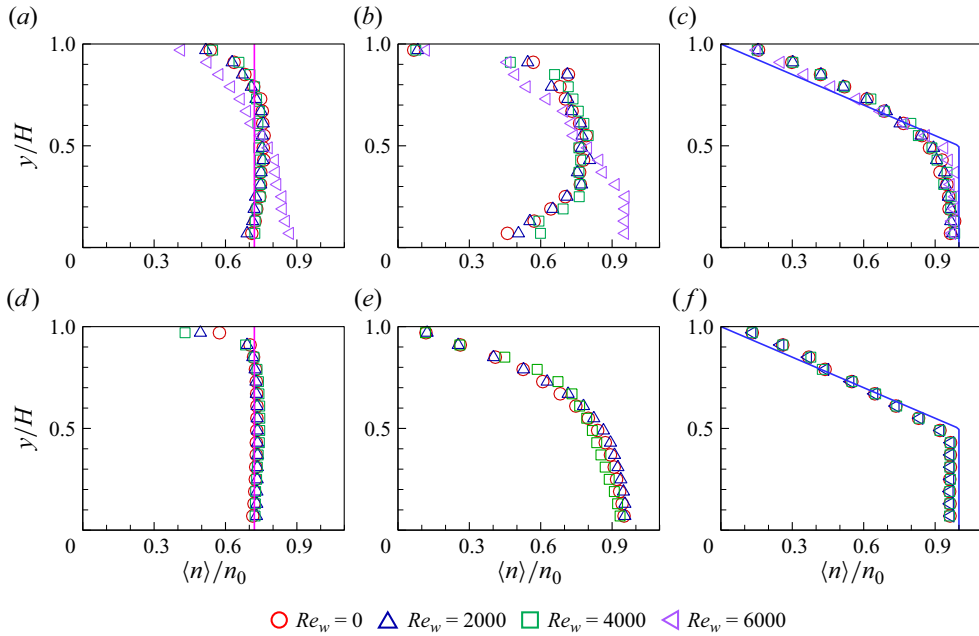


Figure 10. Vertical profiles of the horizontal- and time-averaged local particle concentration obtained from (a–c) the 2-D simulation with  $Ra = 10^8$  and (d–f) the 3-D simulation with  $Ra = 10^7$ . Particle density is fixed as  $\rho_p = 3000 \text{ kg m}^{-3}$ , with diameters of (a,d)  $d_p = 5 \text{ }\mu\text{m}$ , (b,e)  $d_p = 20 \text{ }\mu\text{m}$  and (c,f)  $d_p = 80 \text{ }\mu\text{m}$ . The pink solid line in (a,d) corresponds to (3.7), and the blue solid line in (c,f) corresponds to (3.8).

(i.e. the terminal velocity  $v_t$ ). This explains why the concentration profile for  $Re_w = 6000$  in figure 10(b) is similar to those in figure 10(c) for the 2-D simulation.

### 3.2. Particle deposition on the wall

To quantify the particle deposition behaviour, we first examine the p.d.f.s of their deposition locations along the bottom wall, as shown in figure 11. In our simulations, the particles adhere to the wall upon contact, and we then mark them as deposited and record the contact position as the deposition location. For particles with small  $St$  (see figure 11a), the deposition locations are uniformly distributed along the bottom wall, aligning with the assumption of a spatially uniform particle concentration. For medium  $St$  (see figure 11b), there is pronounced aggregation behaviour for deposition positions along the bottom wall. With the increase of  $Re_w$ , the degree of aggregation weakens, possibly because wall shear causes the boundary layers to move horizontally, thereby dispersing the particles to deposit more evenly along the bottom wall. We also observed a correlation between the regions of particle accumulation on the bottom wall and the rising of hot plumes (compared with figure 2), as revealed in our previous findings (Xu *et al.* 2020) and independent research by Patočka *et al.* (2020, 2022). The accumulation of heavy particles beneath upwellings seems somewhat counterintuitive, as one might expect these particles to accumulate primarily beneath significant downwellings. For large  $St$  (see figure 11c), the uniformity of the deposition pattern is restored, mainly attributed to the reduced influence of the carrier flow on these particles, resulting in an initial uniform distribution less affected by the carrier flow, unlike their low  $St$  counterparts.

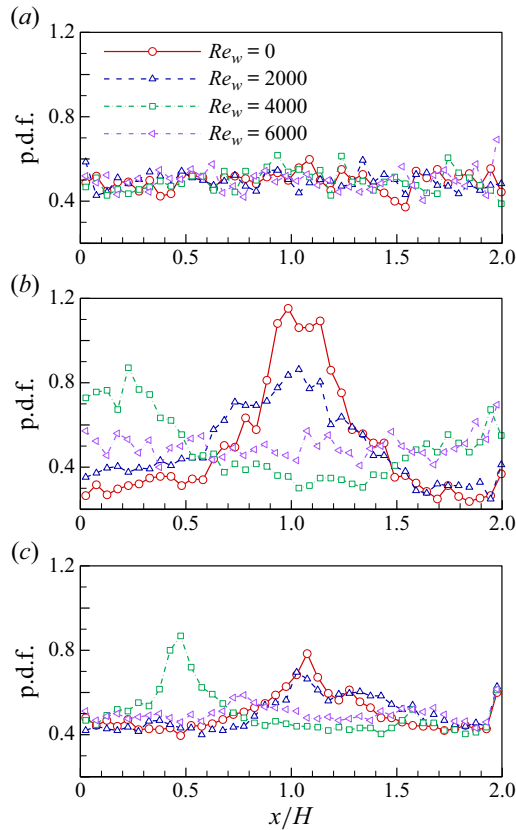


Figure 11. The p.d.f.s of particle deposition locations along the bottom wall with  $Ra = 10^8$ . Particle density is fixed as  $\rho_p = 3000 \text{ kg m}^{-3}$ , with diameters of (a)  $d_p = 5 \mu\text{m}$ , (b)  $d_p = 20 \mu\text{m}$  and (c)  $d_p = 80 \mu\text{m}$ .

We quantify the deposition ratio as the ratio of settled particles  $N_s$  to the initial total number  $N_0$ , and plot the settling curve  $N_s/N_0$  from 2-D simulations as shown in figure 12. For particles with small  $St$ , Martin & Nokes (1989) predicted an exponential deposition rate  $N_s/N_0 = 1 - \exp[-t/(H/v_t)]$ , and our simulation results confirmed the theoretical prediction at  $Re_w \leq 4000$  (see figure 12a,d). However, departure from the expected exponential rate was observed at  $Re_w = 6000$  (see figure 12g), where the LSC was absent and the flow state transitioned to zonal flow. The main reason is that Martin & Nokes (1989) assumed convective velocities were negligible at the bottom boundary layer of the canonical convection cell; in contrast, in the strong wall-sheared convection, horizontal shear velocities persist in the boundary layer, resulting in the failure of the assumption and the deviation in the settling curve. For large  $St$ , a simple model assumes that these particles, being less influenced by the carrier flow, follow a linear deposition rate  $N_s/N_0 = t/(H/v_t)$ . We can see from figure 12(c,f,i) that our simulation results agree with the linear rate at  $t < H/v_t$ , yet deviations are observed at the tails of the settling curve, indicating that a longer time than  $H/v_t$  is required for all the particles to eventually deposit on the wall. A possible explanation is that the carrier flow still has a subtle influence on particles with large  $St$  (yet not infinitely large), and this influence becomes increasingly pronounced as time progresses. In figure 13, we further plot the settling curve  $N_s/N_0$  from 3-D simulations. Overall, the 3-D simulation results reinforce the findings from the 2-D

## Particle transport and deposition

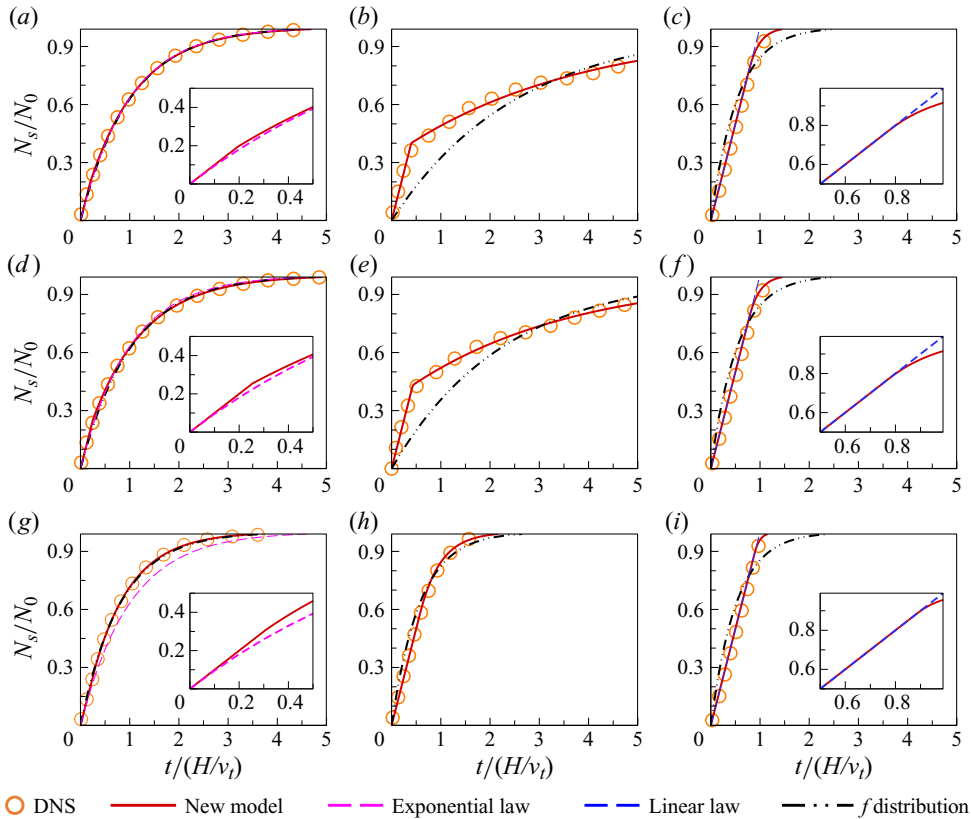


Figure 12. Settling curves from 2-D simulations with  $Ra = 10^8$  at (a–c)  $Re_w = 0$ , (d–f)  $Re_w = 2000$  and (g–i)  $Re_w = 6000$ . Particle density is fixed as  $\rho_p = 3000 \text{ kg m}^{-3}$ , with diameters of (a,d,g)  $d_p = 5 \mu\text{m}$ , (b,e,h)  $d_p = 20 \mu\text{m}$  and (c,f,i)  $d_p = 80 \mu\text{m}$ . The insets in (a,d,g) magnify differences between our new model and the exponential law, and insets in (c,f,i) magnify differences between our new model and the linear law.

simulations that small  $St$  particles settle with an exponential deposition ratio and large  $St$  particles settle with a linear deposition ratio.

Despite existing simple models predicting particle deposition rates for small and large  $St$ , challenges arise for medium  $St$  due to the complex particle–turbulence interactions. Examining the settling curves obtained from simulation, we develop the following model that comprises a linear settling stage succeeded by a nonlinear settling stage. We denote by  $t_s$  the transient time from the linear to the nonlinear stage. At the early settling stage, particles initially released in the lower domain and in the downwelling areas tend to settle. To illustrate this, we conducted an *a posteriori* examination and marked the initial positions of particles that settle during the linear stage, as shown in figure 14(a–c). The particle drift equation (Patočka *et al.* 2022) gives  $\mathbf{u}_p = \mathbf{u}_f + \mathbf{v}_t$  in the limit of  $St \ll 1$ , where  $\mathbf{v}_t$  is the particle Stokes velocity. This equation indicates that particles subjected to updrafts settle at a speed of  $v_t - v_f$ , while those in downdrafts settle at  $v_t + v_f$ . Here,  $v_f$  denotes the vertical flow speed at the particle’s position. At this stage, the settling particles decrease height almost monotonically, without recirculating in the convection cell, as shown in figure 15(a–c). Assuming the same proportion of settling particles affected by the updraft in the lower domain and downdraft in the downwelling areas, then the numbers

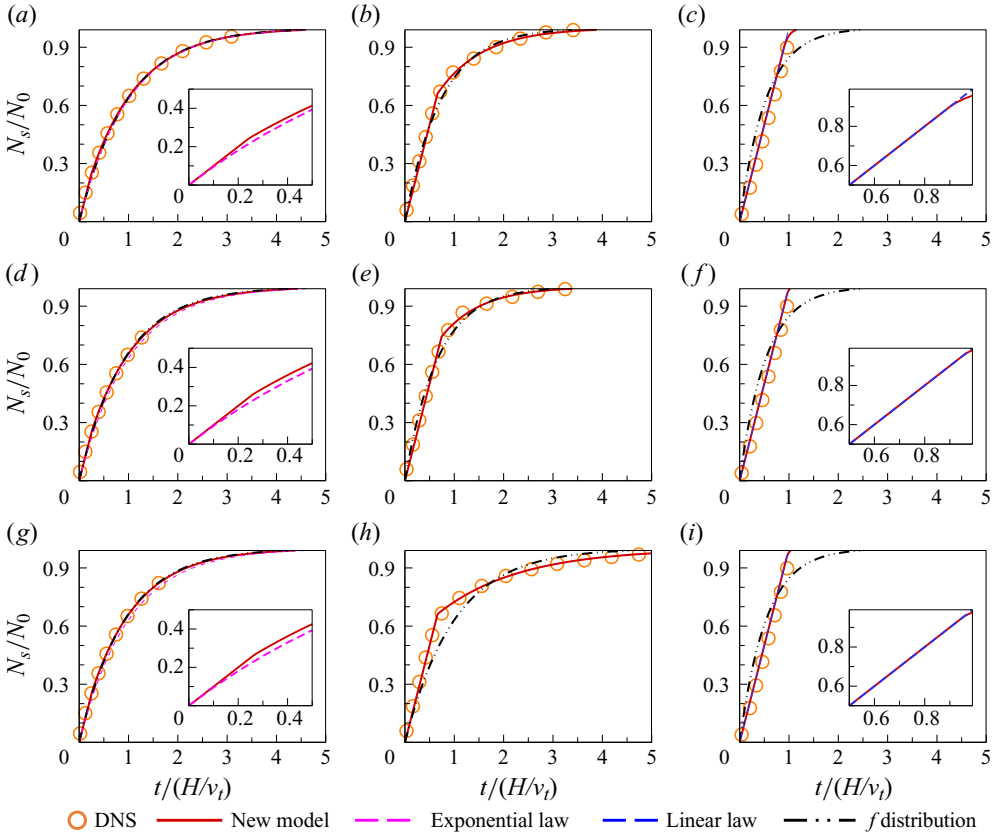


Figure 13. Settling curves from 3-D simulations with  $Ra = 10^7$  at (a–c)  $Re_w = 0$ , (d–f)  $Re_w = 2000$  and (g–i)  $Re_w = 4000$ . Particle density is fixed as  $\rho_p = 3000 \text{ kg m}^{-3}$ , with diameters of (a,d,g)  $d_p = 5 \text{ }\mu\text{m}$ , (b,e,h)  $d_p = 20 \text{ }\mu\text{m}$  and (c,f,i)  $d_p = 80 \text{ }\mu\text{m}$ . The insets in (a,d,g) magnify differences between our new model and the exponential law, and insets in (c,f,i) magnify differences between our new model and the linear law.

of  $N_{up}$  and  $N_{down}$  during  $t \leq t_s$  are

$$N_{up} = \frac{N_0}{2} \frac{(v_t - v_f)tLW}{HLW}, \quad N_{down} = \frac{N_0}{2} \frac{(v_t + v_f)tLW}{HLW}, \quad (3.9a,b)$$

thus, at this settling stage, the deposition ratio (i.e. the fraction of particles that have deposited on the wall relative to the initial number of particles laden in the flow system) is

$$\frac{N_s}{N_0} = \frac{N_{up} + N_{down}}{N_0} = \frac{t}{H/v_t}. \quad (3.10)$$

The above relation indicates that the deposition ratio linearly increases with time, which is why we name it the linear stage.

At the later nonlinear settling stage, particles initially released in the roll centre and upwelling areas tend to settle, as illustrated in figure 14(d–f). The particles circulate within the large-scale roll and may escape the circulation due to small-scale irregularities produced by the emergence of new plumes (Patočka *et al.* 2020). With the increase of wall shear, the lateral motion increases, making the particles more likely to escape the circulation, as shown in figure 15(d–f). Inspired by the stochastic model proposed by Denzel, Bragg & Richter (2023), we denote the time duration for a particle to complete

## Particle transport and deposition

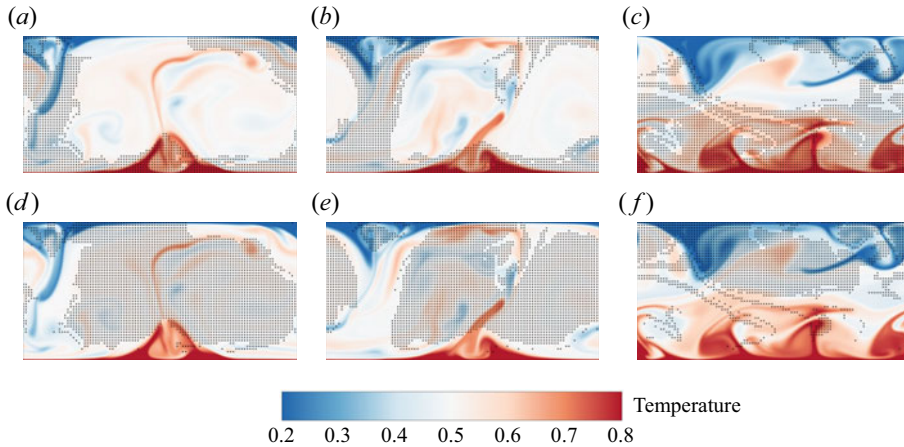


Figure 14. An *a posteriori* examination of the initial positions (black dots) for particles that have settled (*a–c*) during the linear stage and (*d–f*) during the nonlinear stage, alongside the corresponding instantaneous temperature fields (contours) at (*a,d*)  $Re_w = 0$ , (*b,e*)  $Re_w = 2000$  and (*c,f*)  $Re_w = 6000$ , with  $Ra = 10^8$ . Particle density is fixed as  $\rho_p = 3000 \text{ kg m}^{-3}$  and diameter is fixed as  $d_p = 20 \mu\text{m}$ . Note this figure does not represent a ‘real’ instantaneous particle distribution within the convection cell.

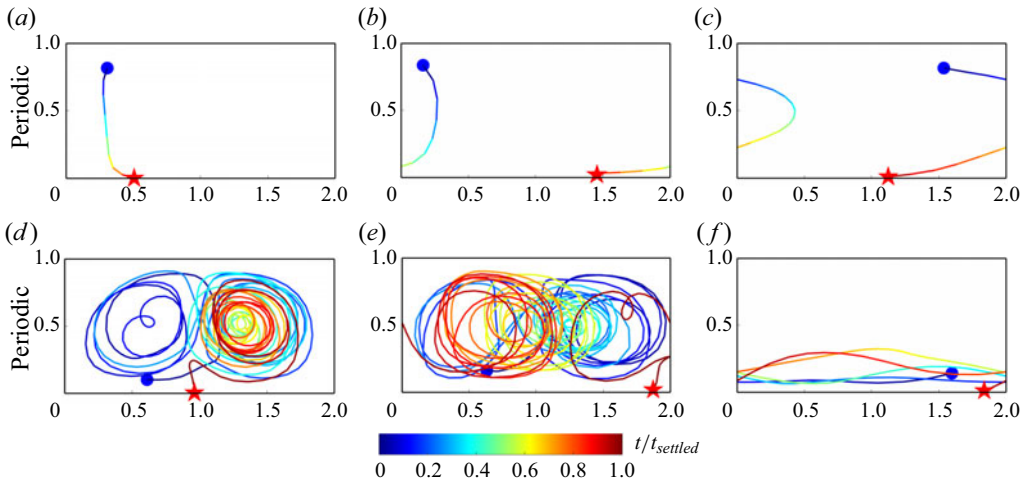


Figure 15. Example particle trajectories for those settled (*a–c*) during the linear stage and (*d–f*) during the nonlinear stage at (*a,d*)  $Re_w = 0$ , (*b,e*)  $Re_w = 2000$  and (*c,f*)  $Re_w = 6000$ , with  $Ra = 10^8$ . Particle density is fixed as  $\rho_p = 3000 \text{ kg m}^{-3}$  and diameter is fixed as  $d_p = 20 \mu\text{m}$ . The trajectories are coloured according to the normalized suspension time of the particles. The blue circle marks the initial position and the red star marks the deposition position.

the circulation as  $t_c$  and the escape probability from the circulation as  $\lambda_f$ . The time decay rate of particle number  $N$  in the convection cell is

$$dN = -\lambda_f \frac{dt}{t_c} N(t) \Rightarrow N(t) = C_0 \exp\left(-\frac{\lambda_f}{t_c} t\right), \quad (3.11)$$

thus, at the nonlinear settling stage, the deposition ratio is

$$\frac{N_s}{N_0} = \frac{N_0 - N}{N_0} = 1 - C_1 \exp\left(-\frac{\lambda_f t}{t_c}\right) = 1 - C_1 \exp\left(-\frac{C_2}{H/v_t} t\right), \quad (3.12)$$

where  $C_1 = C_0/N_0$  and  $C_2 = H\lambda_f/(v_t t_c)$  involves a combination of unknowns  $t_c$  and  $\lambda_f$ .

In short, we propose a new model that describes the settling process via an early linear stage and a later nonlinear stage, written as

$$\frac{N_s}{N_0} = \begin{cases} \frac{t}{H/v_t}, & t \leq t_s \\ 1 - C_1 \exp\left(-\frac{C_2}{H/v_t} t\right), & t \geq t_s. \end{cases} \quad (3.13)$$

Under the assumption of a smooth settling curve, namely  $N_s/N_0$  is continuously changing at  $t_s$ , we then have  $C_1 = [1 - t_s/(H/v_t)]/\exp[-C_2 t_s/(H/v_t)]$ . The determination of  $t_s$  and  $C_2$ , essential for model closure, will be achieved by least square fitting of the settling curves.

Previously, in figures 12 and 13, we compared results from this newly developed model with 2-D and 3-D simulation results, respectively. Good agreement was observed for convective flows across various  $Re_w$  and particles with a wide range of  $St$ . Although our original motivation was to propose a model to predict particle deposition rates for medium  $St$ , the simulation results indicate that our model is applicable for small and large  $St$  as well. In figures 12 and 13, we also plot the predictions from the Patočka *et al.* model (denoted as the  $f$  distribution) (Patočka *et al.* 2020, 2022). The key idea of the  $f$  distribution is to describe particle settling as  $dN/dt = -N(t)/(fH/v_t)$ , leading to a settling curve determined by  $N(t)/N_0 = \exp[-v_t t/(Hf)]$ . We observe a clear departure in the settling curve, mainly because their model adopts a unified exponential solution to describe the settling process, whereas DNS results indicate a linear regime in the settling curves (see also in Patočka *et al.* (2020), figure 3). As acknowledged by Patočka *et al.* (2020), the imperfect fit of the observed settling curves is due to the fact that  $f$  should be a function of time rather than remaining constant. This time dependency of  $f$  results in a misfit between the  $f$  distribution and the observed settling curves, with the largest error occurring for particles with a medium Stokes number. Nevertheless, Patočka *et al.*'s model is still useful for estimating the characteristic time of sedimentation, as discussed later in this paper.

For our new model to be fully closed and predictive, we still need to provide accurate modelling of the parameters  $t_s$  and  $C_2$ . In figure 16, we plot  $t_s$  and  $C_2$  as a function of  $St_f$  for various  $Re_w$  in the 2-D cell with  $Ra = 10^8$ . Here, we adopt  $St_f$  rather than  $St_K$  as the input parameter because  $St_f$  is simpler to determine from the flow parameters, making it more convenient for modelling. In Appendix B we further examine the Rayleigh number dependence of such a relationship with  $Ra = 10^7$  and  $10^9$ . We can see from figure 16(a), for medium  $St_f$  in the range of  $10^{-3} \leq St_f \leq 10^{-2}$ , the parameter  $t_s$  can be empirically estimated as

$$\frac{t_s}{H/v_t} = \begin{cases} 0.47 \log_{10}(St_f) + 1.70, & \text{if large-scale roll} \\ 0.32 \log_{10}(St_f) + 1.50, & \text{if zonal flow.} \end{cases} \quad (3.14)$$

This implies that  $t_s$  is minorly influenced by  $Re_w$  when the convective flow state remains unchanged (either in the LSC or zonal flow state). Practically, to empirically estimate  $t_s$  using the above equation, we should first determine the flow states, then  $t_s$  can be empirically expressed as a function of the Stokes number. This  $t_s$  value is essentially an



## Particle transport and deposition

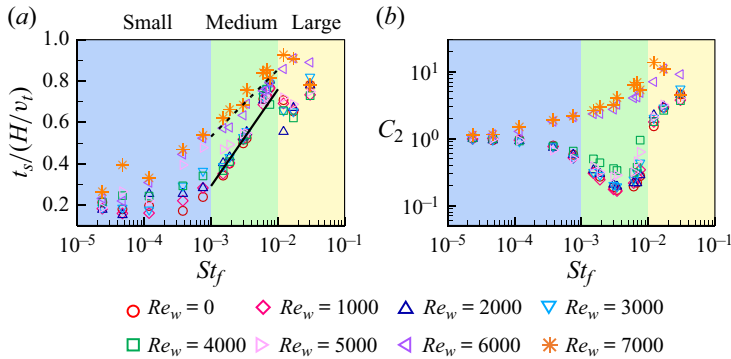


Figure 16. Dependence of the parameters (a)  $t_s$  and (b)  $C_2$  on the Stokes number  $St$  for various wall-shear Reynolds numbers  $Re_w$ , with  $Ra = 10^8$ . The black solid and dashed lines in (a) represent the empirical relations (3.14).

ensemble-averaged value for all the particles. As for the parameter  $C_2$  (see figure 16b), although its original definition is just a combination of unknowns of  $t_c$  and  $\lambda_f$ , for the convenience of mathematical calculation, in the following, we will reveal the physical meaning of this parameter  $C_2$ .

According to the particle mass conservation equation (Martin & Nokes 1989; Patočka *et al.* 2022), the particle deposition rate  $dN/dt$  is equal to the decrease of particle flux  $A_0 v_t n_{bnd}$  at the lower boundary, namely,  $dN/dt = -A_0 v_t n_{bnd}$ . Here,  $A_0$  is the area (or length in the 2-D case) of the bottom boundary, and  $n_{bnd}$  is the mean particle number concentration near the lower boundary. Because the particle deposition rate is

$$\frac{dN}{dt} = \begin{cases} -v_t L \frac{N_0}{LHW}, & t < t_s \\ -v_t LC_2 \frac{N(t)}{LHW}, & t \geq t_s \end{cases} = \begin{cases} -v_t Ln_0, & t \leq t_s \\ -v_t LC_2 \langle n(t) \rangle_V, & t \geq t_s \end{cases}, \quad (3.15)$$

where  $\langle n(t) \rangle_V = N(t)/(LHW)$  is the instantaneous volume-averaged concentration, then we have

$$n_{bnd} = \begin{cases} n_0, & t \leq t_s \\ C_2 \langle n(t) \rangle_V, & t \geq t_s. \end{cases} \quad (3.16)$$

The above analysis indicates that the parameter  $C_2$  describes the ratio of mean particle number concentration near the lower boundary over the volume-averaged particle concentration during the nonlinear stage. From figure 17(a–c), we observe good agreement of the  $C_2$  values calculated via (3.16) with those determined by least square fitting of the settling curves. Then, in figure 17(d–f), we show the settling curves by determining unknown parameters via empirical correlation (3.14) for  $t_s$  and (3.16) for  $C_2$  to close the model. In addition to determining unknown parameters via fitting DNS data, here, we highlight that using these relations provides an alternative solution to predicting the settling curves. Recent work by Denzel *et al.* (2023) also relies on DNS data to determine the input statistics of their model. The difference is that, in Denzel *et al.* (2023), the input parameters for their model are determined from the DNS data as a fit to the cubic splines of the discrete p.d.f.s. for those parameters, while the input parameters for our model are determined from the DNS data as a fit to the settling curves. More importantly, we also demonstrate prediction of the deposition ratio using empirical correlation (3.14) for  $t_s$  and

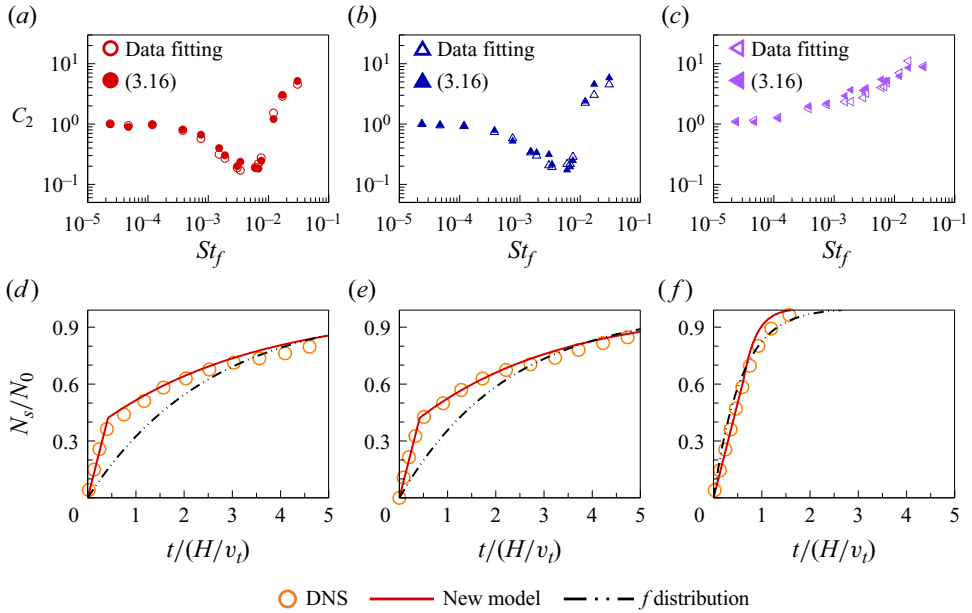


Figure 17. (a–c) The parameter  $C_2$  as a function of  $St$ , determined from data fitting of the settling curves and (3.16). (d–f) Settling curves obtained by determining unknown parameters via (3.14) for  $t_s$  and (3.16) for  $C_2$ , shown for (a,d)  $Re_w = 0$ , (b,e)  $Re_w = 2000$  and (c,f)  $Re_w = 6000$ , with  $Ra = 10^8$ . Particle density is fixed as  $d_p = 3000 \text{ kg m}^{-3}$  and diameter is fixed as  $d_p = 20 \text{ }\mu\text{m}$ .

(3.16) for  $C_2$  to close the model, which provides an alternative solution in addition to fitting DNS data to predict the settling curves.

We finally evaluate our new model in predicting the average residence time  $\overline{t_{res}} = \int_0^\infty N(t) dt / N_0$ , which is the duration that particles spend within the carrier fluid before deposition onto the bottom wall. In figure 18, we plot the average residence time  $\overline{t_{res}}$ , further normalized by the free-fall time  $t_f$ . We can see that our new model is quantitatively accurate for all ranges of  $St$ . For  $St \sim O(10^{-3})$ , the average residence time can exceed the free-fall time  $t_f$  by up to two orders of magnitude. Meanwhile, we calculate the eddy turnover time as  $\tau_e = 2H / \sqrt{\langle v^2 \rangle_{v,t}}$  (Sakievich, Peet & Adrian 2020), which is around  $7.9 t_f$  for  $Ra = 10^7$ ,  $6.6 t_f$  for  $Ra = 10^8$  and  $5.5 t_f$  for  $Ra = 10^9$  when the LSC is present. This suggests that  $\overline{t_{res}}$  is one order of magnitude of higher than  $\tau_e$  and the particles take an average of tens of circulations within the LSC, consistent with the observation of Denzel *et al.* (2023). With the increase of  $St$ , the particle residence time generally decreases. For  $St \sim O(10^{-1})$ , the average residence time of a solid particle is less than the free-fall time for a fluid parcel. Note that, for large  $St$ , the particles' residence time is significantly influenced by their initial positions and velocities; in our simulations, the particles are initially stationary and uniformly distributed. From these results, we can also see that the  $f$  distribution is useful for estimating the mean residence time  $\overline{t_{res}} = \int_0^\infty N(t) dt / N_0 = Hf / v_t$ , which involves the averaged quantity of  $f$  over the entire settling process. This averaging process smooths out the time-dependent variations, providing a good estimate of the mean residence time.

In figure 19, we further plot the residence time normalized by the mean terminal time  $H/v_t$  as a function of  $St$  for various  $Re_w$ . We compare  $\overline{t_{res}}$  with the theoretical values for

Particle transport and deposition

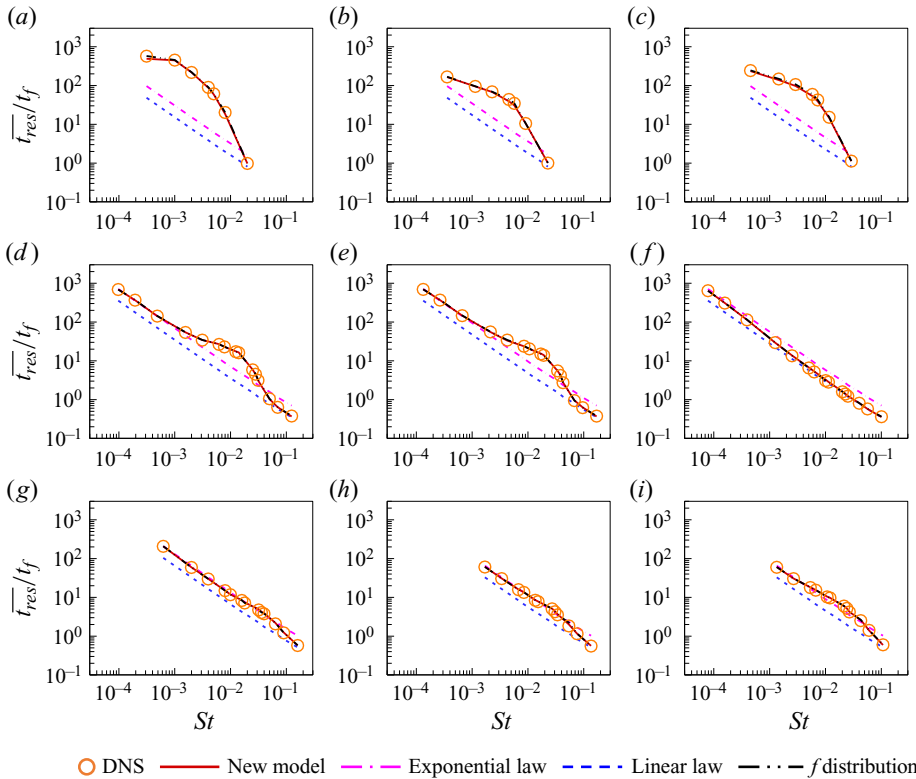


Figure 18. Particle mean residence time  $\overline{t_{res}}$  normalized by the free-fall time  $t_f$ , with (a–c)  $Ra = 10^7$ , (d–f)  $Ra = 10^8$ , (g–i)  $Ra = 10^9$ , at (a)  $Re_w = 0$ , (b)  $Re_w = 1000$ , (c)  $Re_w = 1500$ , (d)  $Re_w = 0$ , (e)  $Re_w = 2000$ , (f)  $Re_w = 6000$ , (g)  $Re_w = 0$ , (h)  $Re_w = 9000$  and (i)  $Re_w = 12000$ .

particles with small  $St$  and large  $St$ , respectively, where

$$\overline{t_{res}} = \begin{cases} \int_0^\infty \exp\left(-\frac{t}{H/v_t}\right) dt = \frac{H}{v_t}, & \text{for small } St \\ \int_0^{H/v_t} \frac{t}{H/v_t} dt = \frac{H}{2v_t}, & \text{for large } St. \end{cases} \quad (3.17)$$

For medium  $St$ , the particles circulate within the LSC, leading to a much longer average residence time compared with the average terminal time. With the increase of  $Ra$ , the LSC becomes more unstable (Zhu *et al.* 2018), and the locking of particles inside the LSC weakens progressively (Patočka *et al.* 2022). For example, at a low  $Ra$  of  $10^7$ , the average residence time can be up to ten times longer than the average terminal time, due to a fraction of particles that are trapped inside the LSC, making the average value large; at a high  $Ra$  of  $10^9$ , the average residence time is only slightly longer than the average terminal time. In addition, under the influence of wall shear, the LSC becomes unstable, leading to a decrease in the average residence time compared with the average terminal time. At  $Ra = 10^8$  and  $Re_w = 6000$  in the 2-D simulations, the updrafts in the zonal flow are much weaker due to the absence of the uplifting force of the plumes. Consequently, we observe faster settling of particles (see figure 19f).

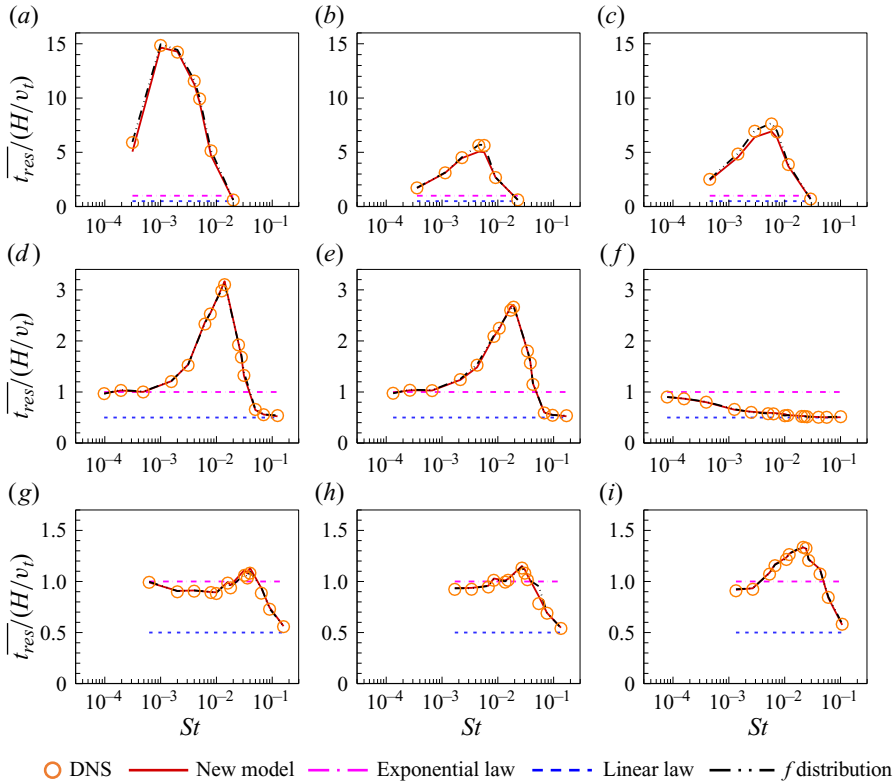


Figure 19. Particle mean residence time  $\overline{t_{res}}$  normalized by the mean terminal time  $H/v_t$ , with (a–c)  $Ra = 10^7$ , (d–f)  $Ra = 10^8$  and (g–i)  $Ra = 10^9$ , at (a)  $Re_w = 0$ , (b)  $Re_w = 1000$ , (c)  $Re_w = 1500$ , (d)  $Re_w = 0$ , (e)  $Re_w = 2000$ , (f)  $Re_w = 6000$ , (g)  $Re_w = 0$ , (h)  $Re_w = 9000$  and (i)  $Re_w = 12000$ .

#### 4. Conclusion

In this work, we have performed DNS of wall-sheared thermal turbulence laden with point particles. We imposed Couette-type shear on the RB convection cell to examine the impact of interactions between vertical buoyancy and horizontal shear forces on particles' motion. We observed that, with the increase of  $Re_w$ , the large-scale rolls expanded horizontally, evolving into zonal flow in 2-D simulations or streamwise-oriented roll in 3-D simulations. For particles with small and medium  $St$ , they either circulate within the LSC when buoyancy dominates or drift near the walls when shear dominates. For large  $St$ , the turbulent flow structure has a minor influence on particles, and they settle almost similarly to those in quiescent fluid environments.

We analysed the particle distribution using Voronoï diagrams and statistical distributions of Voronoï cell areas. For particles with small  $St$ , the Voronoï cells are randomly distributed and exhibit a low degree of aggregation, which is independent of the flow state being either LSC or zonal flow. For medium  $St$ , pronounced spatial inhomogeneity and local preferential concentration are observed. For large  $St$ , clustering also occurs, but wall shear has negligible influence in contrast to cases with medium  $St$ .

We then derive a mathematical model for the particle concentration distribution. For particles with very small  $St$ , we obtain the averaged local particle concentration  $\langle n(y) \rangle_{t_{1/2}}/n_0 = 1/(2 \ln 2)$ . For very large  $St$ , we have  $\langle n(y) \rangle_{t_{1/2}}/n_0 = 2(1 - y/H)$  at  $0.5H \leq y \leq H$  and  $\langle n(y) \rangle_{t_{1/2}}/n_0 = 1$  at  $y \leq 0.5H$ . Compared with the DNS results, for a

small but non-zero  $St$ , the local particle concentration generally agrees with the theoretical predictions when the LSC is present, except there is a reduced number of particles in the upper boundary layer; however, when the flow transitions to zonal flow in 2-D simulations, significant deviation appears. For large but not infinite  $St$ , the local particle concentration generally agrees with theoretical prediction across all  $Re_w$ , highlighting again that the particles' motion is nearly unaffected by the turbulent flow state.

We further plot the settling curves to quantify the deposition ratio. Good agreement is observed between the DNS results and previous theoretical predictions in the small and large  $St$  regimes, namely, for small  $St$  with an exponential deposition ratio and for large  $St$  with a linear deposition ratio. For medium  $St$ , to bridge the gap, we develop a new model that describes the settling process via an early linear stage and a later nonlinear stage. At the early linear settling stage, particles initially released in the lower domain and in the downwelling areas settle. Specifically, the same proportion of particles in the updraft and downdraft regions settle with a speed of  $v_t - v_f$  and  $v_t + v_f$ , respectively, leading to the deposition ratio  $N_s/N_0 = t/(H/v_t)$ . At the later nonlinear settling stage, particles circulate within the convection cell during  $t_c$  and may escape the circulation with a probability of  $\lambda_f$ , leading to the deposition ratio  $N_s/N_0 = 1 - C_1 \exp[-C_2 t/(H/v_t)]$ . The unknowns in our model can be determined either by least square fitting of the settling curves, or by our empirical relations (3.14) and (3.16). In addition, we found that our model for particle deposition is also accurate in predicting the average residence time across a wide range of  $St$  for various  $Re_w$ .

**Supplementary material and movies.** Supplementary material and movies are available at <https://doi.org/10.1017/jfm.2024.936>.

**Funding.** This work was supported by the National Natural Science Foundation of China (NSFC) through grants nos 12272311, 12125204 and 12388101, the Young Elite Scientists Sponsorship Program by CAST (2023QNRC001) and the 111 project of China (no. B17037).

**Declaration of interests.** The authors report no conflict of interest.

**Author ORCIDs.**

 Ao Xu <https://orcid.org/0000-0003-0648-2701>;

 Heng-Dong Xi <https://orcid.org/0000-0002-2999-2694>.

## Appendix A. Spatial distribution of local Kolmogorov length scale

In the main text, we presented the Kolmogorov length scale based on the volume- and time-averaged method. Here, we further present the time-averaged local Kolmogorov length scale distribution  $\langle \eta_K \rangle_t$ . The local Kolmogorov length scale is calculated as  $\eta_K(\mathbf{x}, t) = [v^3/\varepsilon_u(\mathbf{x}, t)]^{1/4}$  (Shishkina *et al.* 2010). Taking  $Ra = 10^8$  as an example, we can see from figure 20 that the minimal local Kolmogorov length scale is around  $480 \mu\text{m}$ , which is six times larger than the largest particle diameter of  $d_p = 80 \mu\text{m}$ . This indicates that the point-particle model can be safely used.

## Appendix B. Rayleigh number dependence of parameters $t_s$ and $C_2$

In addition to figure 16, we further examine the Rayleigh number dependence of parameters  $t_s$  and  $C_2$ . In figures 21 and 22, we present the parameters  $t_s$  and  $C_2$  as functions of the Stokes number  $St$  for various wall-shear Reynolds numbers  $Re_w$  with  $Ra = 10^7$  and  $Ra = 10^9$ , respectively. The results demonstrate that our empirical relations (3.14) can also be applied for a wide range of  $Ra$ .

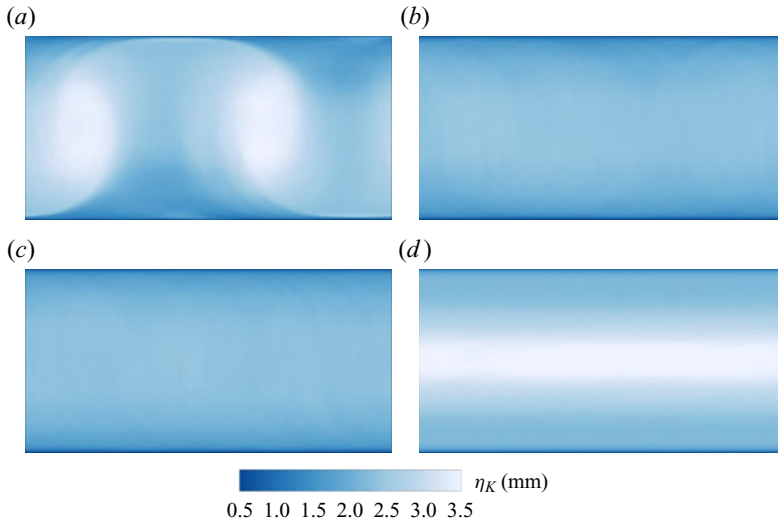


Figure 20. Spatial distribution of time-averaged local Kolmogorov length scale  $\langle \eta_K \rangle_t$  at (a)  $Re_w = 0$ , (b)  $Re_w = 2000$ , (c)  $Re_w = 4000$  and (d)  $Re_w = 6000$ , with  $Ra = 10^8$  and  $Pr = 0.71$  (see table 1 in the main text for the corresponding fluid properties).

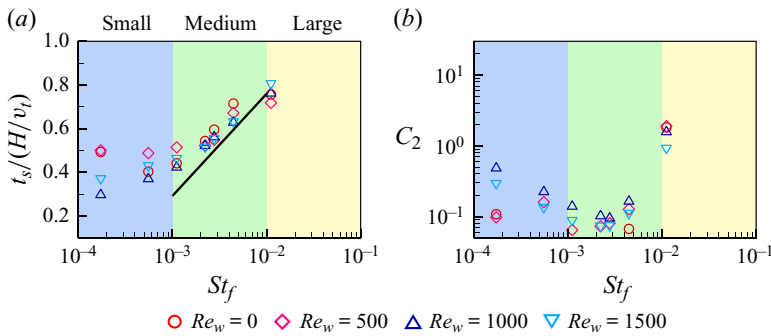


Figure 21. Dependence of the parameters (a)  $t_s$  and (b)  $C_2$  on the Stokes number  $St$  for various wall-shear Reynolds numbers  $Re_w$  with  $Ra = 10^7$ . The black solid lines in (a) represent the empirical relations (3.14).

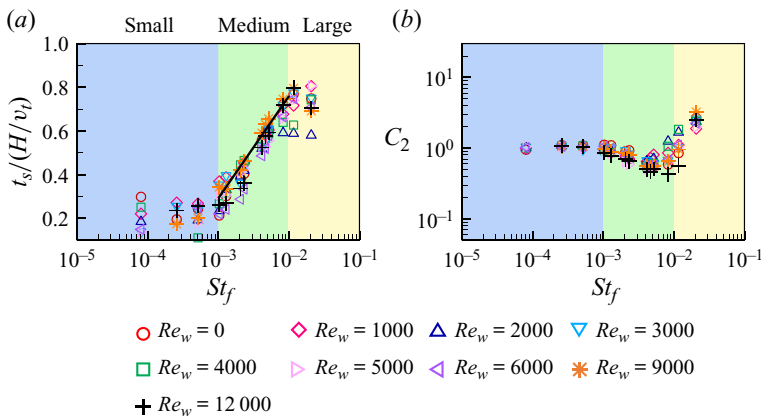


Figure 22. Dependence of (a)  $t_s$  and (b)  $C_2$  on  $St$  for various  $Re_w$  with  $Ra = 10^9$ . The black solid lines in (a) represent the empirical relations (3.14).

## REFERENCES

- AHLERS, G., GROSSMANN, S. & LOHSE, D. 2009 Heat transfer and large scale dynamics in turbulent Rayleigh–Bénard convection. *Rev. Mod. Phys.* **81** (2), 503–537.
- BALACHANDAR, S. & EATON, J.K. 2010 Turbulent dispersed multiphase flow. *Annu. Rev. Fluid Mech.* **42**, 111–133.
- BATCHELOR, G.K. 1959 Small-scale variation of convected quantities like temperature in turbulent fluid. Part 1. General discussion and the case of small conductivity. *J. Fluid Mech.* **5** (1), 113–133.
- BERNARDINI, M., PIROZZOLI, S. & ORLANDI, P. 2014 Velocity statistics in turbulent channel flow up to  $Re_\tau = 4000$ . *J. Fluid Mech.* **742**, 171–191.
- BLASS, A., TABAK, P., VERZICCO, R., STEVENS, R.J.A.M. & LOHSE, D. 2021 The effect of Prandtl number on turbulent sheared thermal convection. *J. Fluid Mech.* **910**, A37.
- BLASS, A., ZHU, X.-J., VERZICCO, R., LOHSE, D. & STEVENS, R.J.A.M. 2020 Flow organization and heat transfer in turbulent wall sheared thermal convection. *J. Fluid Mech.* **897**, A22.
- BOSSE, T., KLEISER, L. & MEIBURG, E. 2006 Small particles in homogeneous turbulence: settling velocity enhancement by two-way coupling. *Phys. Fluids* **18** (2), 027102.
- BRANDT, L. & COLETTI, F. 2022 Particle-laden turbulence: progress and perspectives. *Annu. Rev. Fluid Mech.* **54**, 159–189.
- CALZAVARINI, E., JIANG, L.-F. & SUN, C. 2020 Anisotropic particles in two-dimensional convective turbulence. *Phys. Fluids* **32** (2), 023305.
- CALZAVARINI, E., KERSCHER, M., LOHSE, D. & TOSCHI, F. 2008 Dimensionality and morphology of particle and bubble clusters in turbulent flow. *J. Fluid Mech.* **607**, 13–24.
- CHALLABOTLA, N.R., ZHAO, L.-H. & ANDERSSON, H.I. 2015 Orientation and rotation of inertial disk particles in wall turbulence. *J. Fluid Mech.* **766**, R2.
- CHEN, X.-Y. & PROSPERETTI, A. 2024 Particle-resolved multiphase Rayleigh–Bénard convection. *Phys. Rev. Fluids* **9** (5), 054301.
- CHILLÀ, F. & SCHUMACHER, J. 2012 New perspectives in turbulent Rayleigh–Bénard convection. *Eur. Phys. J. E* **35** (58), 1–25.
- CLIFT, R., GRACE, J.R. & WEBER, M.E. 1978 *Bubbles, Drops, and Particles*. Academic Press.
- DEMOU, A.D., ARDEKANI, M.N., MIRBOD, P. & BRANDT, L. 2022 Turbulent Rayleigh–Bénard convection in non-colloidal suspensions. *J. Fluid Mech.* **945**, A6.
- DENZEL, C.J., BRAGG, A.D. & RICHTER, D.H. 2023 Stochastic model for the residence time of solid particles in turbulent Rayleigh–Bénard flow. *Phys. Rev. Fluids* **8** (2), 024307.
- DU, Y.-H. & YANG, Y.-T. 2022 Wall-bounded thermal turbulent convection driven by heat-releasing point particles. *J. Fluid Mech.* **953**, A41.
- FERENC, J.S. & NÉDA, Z. 2007 On the size distribution of Poisson Voronoi cells. *Physica A* **385** (2), 518–526.
- FISCHER, P.F. 1997 An overlapping Schwarz method for spectral element solution of the incompressible Navier–Stokes equations. *J. Comput. Phys.* **133** (1), 84–101.
- GAO, W., SAMTANEY, R. & RICHTER, D.H. 2023 Direct numerical simulation of particle-laden flow in an open channel at  $Re_\tau = 5186$ . *J. Fluid Mech.* **957**, A3.
- GOLUSKIN, D., JOHNSTON, H., FLIERL, G.R. & SPIEGEL, E.A. 2014 Convectively driven shear and decreased heat flux. *J. Fluid Mech.* **759**, 360–385.
- GORE, R.A. & CROWE, C.T. 1989 Effect of particle size on modulating turbulent intensity. *Intl J. Multiphase Flow* **15** (2), 279–285.
- GUHA, A. 2008 Transport and deposition of particles in turbulent and laminar flow. *Annu. Rev. Fluid Mech.* **40**, 311–341.
- HEDWORTH, H.A., KARAM, M., MCCONNELL, J., SUTHERLAND, J.C. & SAAD, T. 2021 Mitigation strategies for airborne disease transmission in orchestras using computational fluid dynamics. *Sci. Adv.* **7** (26), eabg4511.
- VAN DER HOEF, M.A., VAN SINT ANNALAND, M., DEEN, N.G. & KUIPERS, J.A.M. 2008 Numerical simulation of dense gas-solid fluidized beds: a multiscale modeling strategy. *Annu. Rev. Fluid Mech.* **40**, 47–70.
- HORI, K., JONES, C.A., ANTUÑANO, A., FLETCHER, L.N. & TOBIAS, S.M. 2023 Jupiter’s cloud-level variability triggered by torsional oscillations in the interior. *Nat. Astron.* **7** (7), 825–835.
- JIE, Y.-C., CUI, Z.-W., XU, C.-X. & ZHAO, L.-H. 2022 On the existence and formation of multi-scale particle streaks in turbulent channel flows. *J. Fluid Mech.* **935**, A18.
- JIN, T.-C., WU, J.-Z., ZHANG, Y.-Z., LIU, Y.-L. & ZHOU, Q. 2022 Shear-induced modulation on thermal convection over rough plates. *J. Fluid Mech.* **936**, A28.

- KOOIJ, G.L., BOTCHEV, M.A., FREDERIX, E.M.A., GEURTS, B.J., HORN, S., LOHSE, D., VAN DER POEL, E.P., SHISHKINA, O., STEVENS, R.J.A.M. & VERZICCO, R. 2018 Comparison of computational codes for direct numerical simulations of turbulent Rayleigh–Bénard convection. *Comput. Fluids* **166**, 1–8.
- LI, J.-Y. & YANG, Y.-T. 2022 Flow structures and vertical transport in tilting salt fingers with a background shear. *Phys. Rev. Fluids* **7** (5), 053501.
- LI, Y.-Z., CHEN, X., XU, A. & XI, H.-D. 2022 Counter-flow orbiting of the vortex centre in turbulent thermal convection. *J. Fluid Mech.* **935**, A19.
- LIN, Y.-F. & JACKSON, A. 2021 Large-scale vortices and zonal flows in spherical rotating convection. *J. Fluid Mech.* **912**, A46.
- LOHSE, D. & XIA, K.-Q. 2010 Small-scale properties of turbulent Rayleigh–Bénard convection. *Annu. Rev. Fluid Mech.* **42**, 335–364.
- MARTIN, D. & NOKES, R. 1989 A fluid-dynamical study of crystal settling in convecting magmas. *J. Petrol.* **30** (6), 1471–1500.
- MATHAI, V., LOHSE, D. & SUN, C. 2020 Bubbly and buoyant particle-laden turbulent flows. *Annu. Rev. Condens. Matter Phys.* **11**, 529–559.
- MAXEY, M. 2017 Simulation methods for particulate flows and concentrated suspensions. *Annu. Rev. Fluid Mech.* **49**, 171–193.
- MITTAL, R., NI, R. & SEO, J.H. 2020 The flow physics of COVID-19. *J. Fluid Mech.* **894**, F2.
- MONCHAUX, R., BOURGOIN, M. & CARTELLIER, A. 2010 Preferential concentration of heavy particles: a Voronoi analysis. *Phys. Fluids* **22** (10), 103304.
- MONCHAUX, R., BOURGOIN, M. & CARTELLIER, A. 2012 Analyzing preferential concentration and clustering of inertial particles in turbulence. *Intl J. Multiphase Flow* **40**, 1–18.
- MOTOORI, Y., WONG, C.K. & GOTO, S. 2022 Role of the hierarchy of coherent structures in the transport of heavy small particles in turbulent channel flow. *J. Fluid Mech.* **942**, A3.
- ORESTA, P. & PROSPERETTI, A. 2013 Effects of particle settling on Rayleigh–Bénard convection. *Phys. Rev. E* **87** (6), 063014.
- PARK, H.J., O’KEEFE, K. & RICHTER, D.H. 2018 Rayleigh–Bénard turbulence modified by two-way coupled inertial, nonisothermal particles. *Phys. Rev. Fluids* **3** (3), 034307.
- PATOČKA, V., CALZAVARINI, E. & TOSI, N. 2020 Settling of inertial particles in turbulent Rayleigh–Bénard convection. *Phys. Rev. Fluids* **5** (11), 114304.
- PATOČKA, V., TOSI, N. & CALZAVARINI, E. 2022 Residence time of inertial particles in 3D thermal convection: implications for magma reservoirs. *Earth Planet. Sci. Lett.* **591**, 117622.
- PIROZZOLI, S., BERNARDINI, M., VERZICCO, R. & ORLANDI, P. 2017 Mixed convection in turbulent channels with unstable stratification. *J. Fluid Mech.* **821**, 482–516.
- SAKIEVICH, P.J., PEET, Y.T. & ADRIAN, R.J. 2020 Temporal dynamics of large-scale structures for turbulent Rayleigh–Bénard convection in a moderate aspect-ratio cylinder. *J. Fluid Mech.* **901**, A31.
- SHISHKINA, O., STEVENS, R.J.A.M., GROSSMANN, S. & LOHSE, D. 2010 Boundary layer structure in turbulent thermal convection and its consequences for the required numerical resolution. *New J. Phys.* **12** (7), 075022.
- SILANO, G., SREENIVASAN, K.R. & VERZICCO, R. 2010 Numerical simulations of Rayleigh–Bénard convection for Prandtl numbers between  $10^{-1}$  and  $10^4$  and Rayleigh numbers between  $10^5$  and  $10^9$ . *J. Fluid Mech.* **662**, 409–446.
- STEVENS, R.J.A.M., BLASS, A., ZHU, X.-J., VERZICCO, R. & LOHSE, D. 2018 Turbulent thermal superstructures in Rayleigh–Bénard convection. *Phys. Rev. Fluids* **3** (4), 041501.
- SUN, D.-F., WAN, Z.-H. & SUN, D.-J. 2024 Modulation of Rayleigh–Bénard convection with a large temperature difference by inertial nonisothermal particles. *Phys. Fluids* **36** (1), 017135.
- TAGAWA, Y., MERCADO, J.M., PRAKASH, V.N., CALZAVARINI, E., SUN, C. & LOHSE, D. 2012 Three-dimensional Lagrangian Voronoi analysis for clustering of particles and bubbles in turbulence. *J. Fluid Mech.* **693**, 201–215.
- TEIMURAZOV, A., SINGH, S., SU, S., ECKERT, S., SHISHKINA, O. & VOGT, T. 2023 Oscillatory large-scale circulation in liquid-metal thermal convection and its structural unit. *J. Fluid Mech.* **977**, A16.
- TOSCHI, F. & BODENSCHATZ, E. 2009 Lagrangian properties of particles in turbulence. *Annu. Rev. Fluid Mech.* **41**, 375–404.
- VOGT, T., HORN, S., GRANNAN, A.M. & AURNOU, J.M. 2018 Jump rope vortex in liquid metal convection. *Proc. Natl Acad. Sci. USA* **115** (50), 12674–12679.
- WANG, B.-F., ZHOU, Q. & SUN, C. 2020a Vibration-induced boundary-layer destabilization achieves massive heat-transport enhancement. *Sci. Adv.* **6** (21), eaaz8239.
- WANG, L.-P. & MAXEY, M.R. 1993 Settling velocity and concentration distribution of heavy particles in homogeneous isotropic turbulence. *J. Fluid Mech.* **256**, 27–68.



- WANG, Q., CHONG, K.-L., STEVENS, R.J.A.M., VERZICCO, R. & LOHSE, D. 2020*b* From zonal flow to convection rolls in Rayleigh–Bénard convection with free-slip plates. *J. Fluid Mech.* **905**, A21.
- WINCHESTER, P., DALLAS, V. & HOWELL, P.D. 2021 Zonal flow reversals in two-dimensional Rayleigh–Bénard convection. *Phys. Rev. Fluids* **6** (3), 033502.
- XI, H.-D., LAM, S. & XIA, K.-Q. 2004 From laminar plumes to organized flows: the onset of large-scale circulation in turbulent thermal convection. *J. Fluid Mech.* **503**, 47–56.
- XIA, K.-Q., HUANG, S.-D., XIE, Y.-C. & ZHANG, L. 2023 Tuning heat transport via coherent structure manipulation: recent advances in thermal turbulence. *Nat. Sci. Rev.* **10** (6), nwad012.
- XU, A. & LI, B.-T. 2023 Multi-GPU thermal lattice Boltzmann simulations using OpenACC and MPI. *Intl J. Heat Mass Transfer* **201**, 123649.
- XU, A., SHI, L. & ZHAO, T.-S. 2017 Accelerated lattice Boltzmann simulation using GPU and OpenACC with data management. *Intl J. Heat Mass Transfer* **109**, 577–588.
- XU, A., TAO, S., SHI, L. & XI, H.-D. 2020 Transport and deposition of dilute microparticles in turbulent thermal convection. *Phys. Fluids* **32** (8), 083301.
- XU, A., XU, B.-R. & XI, H.-D. 2023 Wall-sheared thermal convection: heat transfer enhancement and turbulence relaminarization. *J. Fluid Mech.* **960**, A2.
- YANG, W.-W., WAN, Z.-H., ZHOU, Q. & DONG, Y.-H. 2022*a* On the energy transport and heat transfer efficiency in radiatively heated particle-laden Rayleigh–Bénard convection. *J. Fluid Mech.* **953**, A35.
- YANG, W.-W., ZHANG, Y.-Z., WANG, B.-F., DONG, Y.-H. & ZHOU, Q. 2022*b* Dynamic coupling between carrier and dispersed phases in Rayleigh–Bénard convection laden with inertial isothermal particles. *J. Fluid Mech.* **930**, A24.
- YERRAGOLAM, G.S., VERZICCO, R., LOHSE, D. & STEVENS, R.J.A.M. 2022 How small-scale flow structures affect the heat transport in sheared thermal convection. *J. Fluid Mech.* **944**, A1.
- ZHANG, H. 2024 Structure and coupling characteristics of multiple fields in dust storms. *Acta Mechanica Sin.* **40**, 123339.
- ZHANG, H., CUI, Y.-K. & ZHENG, X.-J. 2023 How electrostatic forces affect particle behaviour in turbulent channel flows. *J. Fluid Mech.* **967**, A8.
- ZHANG, X., VAN GILS, D.P.M., HORN, S., WEDI, M., ZWIRNER, L., AHLERS, G., ECKE, R.E., WEISS, S., BODENSCHATZ, E. & SHISHKINA, O. 2020 Boundary zonal flow in rotating turbulent Rayleigh–Bénard convection. *Phys. Rev. Lett.* **124** (8), 084505.
- ZHENG, X.-J. 2009 *Mechanics of Wind-Blown Sand Movements*. Springer Science and Business Media.
- ZHOU, Q., SUN, C. & XIA, K.-Q. 2007 Morphological evolution of thermal plumes in turbulent Rayleigh–Bénard convection. *Phys. Rev. Lett.* **98** (7), 074501.
- ZHU, X.-J., MATHAI, V., STEVENS, R.J.A.M., VERZICCO, R. & LOHSE, D. 2018 Transition to the ultimate regime in two-dimensional Rayleigh–Bénard convection. *Phys. Rev. Lett.* **120** (14), 144502.
- ZWICK, D. 2019 ppicf: a parallel particle-in-cell library in Fortran. *J. Open Source Softw.* **4** (37), 1400.